UCLA
UCLA Previously Published Works

Title

Thermal nature and resolution of the lithosphere–asthenosphere boundary under the Pacific from surface waves

Permalink

https://escholarship.org/uc/item/4kz6j2br

Journal

Geophysical Journal International, 216(2)

ISSN

0956-540X

Authors

Beghein, C
Xing, Z
Goes, S

Publication Date

2019-02-01

DOI

10.1093/gji/ggy490

Peer reviewed

eScholarship.org Powered by the California Digital Library
University of California

Geophysical Journal International

Geophys. J. Int. (2019) **216,** 1441–1465
Advance Access publication 2018 November 21
GJI Seismology

doi: 10.1093/gji/ggy490

Thermal nature and resolution of the lithosphere–asthenosphere boundary under the Pacific from surface waves

C. Beghein [1,2] Z. Xing[1] and S. Goes[3]

[1] *Department of Earth, Planetary, and Space Sciences, University of California Los Angeles, CA* 90095*, USA. E-mail: cbeghein@epss.ucla.edu*
[2] *Lunar and Planetary Institute, Houston, TX* 77058*, USA*
[3] *Department of Earth Science and Engineering, Faculty of Engineering, Imperial College, London SW7 2AZ, UK*

Accepted 2018 November 20. Received 2018 November 8; in original form 2018 July 14

SUMMARY

It is strongly debated whether the interface between the lithosphere and underlying asthenosphere is a temperature-dependent rheological transition, as expected in a thermal convection system, or additionally affected by the presence of melts and/or fluids. Previous surface wave studies of Pacific oceanic lithosphere have found that shear velocity and azimuthal anisotropy vary with seafloor crustal age as expected for a thermal control; however radial anisotropy does not. Various thermomechanical models have been proposed to explain this disparate behaviour. Nonetheless, it is unclear how robust the surface wave constraints are, and this is what we test in this study. We apply a Bayesian model space search approach to three published Pacific surface wave dispersion data sets, two phase-velocity and one combined phase- and group-velocity set, and determine various proxies for the depth of the lithosphere–asthenosphere boundary (LAB) and their uncertainties based on the velocity and radial anisotropy model distributions obtained. In their overall character and pattern with age, the velocity models from different data sets are consistent with each other, although they differ in their values of LAB depths. Uncertainties are substantial (as much as 20 km on LAB depths) and the addition of group-velocity data does not reduce them. Radial anisotropy structures differ even in pattern and display no obvious age dependence. However, given the uncertainties, we cannot exclude that radial anisotropy, azimuthal anisotropy and velocity models actually reflect compatible, age-dependent, LAB depth estimates. The velocity LAB trends are most like those expected for half-space cooling, because velocity differences persist at old ages, below the depth of common plate cooling models. Any direct signature of sub-ridge melt would be too small-scale to be resolved by these data. However, the velocity-increasing effects of dehydration and depletion due to melting below the ridge could explain why LAB proxy depths tend to a minimum of ∼60 km below young ocean floor.

Key words: Inverse theory; Probability distributions; Tomography; Seismic anisotropy; Statistical seismology; Surface waves and free oscillations.

1 INTRODUCTION

The transition from the lithosphere, the mechanically strong plate at the surface, to the deeper and more ductile asthenosphere, is key to better understand plate tectonics on Earth and our planet's thermochemical evolution. However, the nature of this transition, often called the LAB (lithosphere–asthenosphere boundary), remains elusive as several factors such as temperature, chemical composition, partial melt, water content and grain size may affect the magnitude and sharpness of this rheological contrast (see review by Fischer *et al.* 2010). Constraining the depth of the LAB and how it varies between tectonic blocks or with ocean crustal age can help determine the relative importance of these factors.

A variety of geological, geochemical and geophysical observables can be used to obtain information about the LAB (Eaton *et al.* 2009) and to determine its depth. However, different proxies can lead to different conclusions. For instance, seafloor magnetotelluric studies reveal the presence of a high-conductivity layer beneath the lithosphere (Filloux 1980; Chave *et al.* 1981; Lizarralde *et al.* 1995; Naif *et al.* 2013). Several authors have favoured the presence of partial melt to explain these observations (Shankland *et al.* 1981; Naif *et al.* 2013), although some have suggested that the presence of water is responsible (Lizarralde *et al.* 1995). Based on their measurements, Naif *et al.* (2013)

© The Author(s) 2018. Published by Oxford University Press on behalf of The Royal Astronomical Society.

Downloaded from https://academic.oup.com/gji/article-abstract/216/2/1441/5195529 by University of California, Los Angeles user on 06 February 2019

additionally proposed that the LAB under young oceanic plates consists of a thin, partially molten, low-viscosity layer located between 45 and 70 km, and acts as a lubricant, enhancing decoupling of the overlying lithosphere from the convecting mantle.

Seismological studies can also be used to constrain the depth of the LAB, but results and their interpretation vary as well. The top of the asthenosphere is often associated with a sharp decrease of several per cent in wave velocity. It is called the Gutenberg discontinuity in oceanic settings where it has been observed with SS precursor data, and with ScS and sScS reflected waves (Revenaugh & Jordan 1991; Gaherty *et al.* 1996; Bagley & Revenaugh 2008; Rychert & Shearer 2011; Schmerr 2012; Tharimena *et al.* 2017a). It can also be observed with receiver functions, but their usage is mostly limited to continents, ocean islands and ocean bottom seismometers because it can only map reflectors located underneath a seismic station (Kawakatsu *et al.* 2009; Courtier & Leahy 2011). The sharpness and lack of clear crustal age dependence of this discontinuity, at least for ages >36 Myr (Tharimena *et al.* 2017a), call for a compositional origin of the observed discontinuities. Partial melt as well as the effect of dehydration at the ridge have been invoked to explain these observations (Anderson & Sammis 1970; Gaherty *et al.* 1996; Hirth & Kohlstedt 1996; Karato & Jung 1998; Kawakatsu *et al.* 2009; Karato 2012; Schmerr 2012; Sakamaki *et al.* 2013; Olugboji *et al.* 2016; Tharimena *et al.* 2017a). Melt is also often invoked to explain the origin of the discontinuity in continents (Tharimena *et al.* 2017b).

By contrast, surface wave tomography has yielded shear wave velocity and azimuthal anisotropy models under oceans that display a dependence on seafloor age, suggesting that oceanic plate formation is primarily controlled by temperature (Nishimura & Forsyth 1989; Ritzwoller *et al.* 2004; Maggi *et al.* 2006; Nettles & Dziewoński 2008; Debayle & Ricard 2013; Becker *et al.* 2014; Beghein *et al.* 2014; Burgos *et al.* 2014; Schaeffer *et al.* 2016; Ma & Dalton 2017). These models resolve a relatively high-velocity layer atop a low-velocity zone (Nishimura & Forsyth 1989; Maggi *et al.* 2006; Nettles & Dziewoński 2008; Debayle & Ricard 2013; Becker *et al.* 2014; Beghein *et al.* 2014; Burgos *et al.* 2014; Schaeffer *et al.* 2016). In many cases, the thickness of the top layer increases with the age of the ocean crust, following to first order a half-space cooling (HSC) model, in which thickness increases with the square root of age (Parsons & Sclater 1977). In a few cases, a plate cooling model, where the thickness at older ages is limited to a maximum of around 100 km by either small-scale instabilities or reheating (Stein & Stein 1992) was found to be a better fit to both the seismic data and seafloor topography (Ritzwoller *et al.* 2004; Ma & Dalton 2017). Azimuthal anisotropy models derived from surface waves are often characterized by two layers, with fast axes that follow ocean ridge paleospreading directions in the top layer and parallel to the geodetically determined present-day direction of plate motion (Gripp & Gordon 1990, 1992) in the lower layer (Smith *et al.* 2004; Maggi *et al.* 2006; Debayle & Ricard 2013; Becker *et al.* 2014; Beghein *et al.* 2014; Burgos *et al.* 2014; Schaeffer *et al.* 2016). In addition, the depth at which the azimuthal anisotropy is well aligned with the plate motion direction increases with plate age and tends to display a HSC age dependence (e.g. Debayle & Ricard 2013; Beghein *et al.* 2014).

Interestingly, however, three radial anisotropy models published in the last decade and resulting from regularized inversions of surface wave data do not display the same age dependence as their isotropic or azimuthally anisotropic counterparts (Nettles & Dziewoński 2008; Beghein *et al.* 2014; Burgos *et al.* 2014). Instead, they tend to be characterized by an upper layer where $V_{SV} > V_{SH}$ and a lower layer where $V_{SV} < V_{SH}$, with a transition that occurs at the same depth of ∼60–80 km for all ages, that is, it does not show any significant age dependence. Lattice-preferred orientation (LPO) of olivine is thought to be the primary contribution to the seismic anisotropy observed in the upper mantle. Laboratory experiments show that, in most cases, when an aggregate of olivine crystals is deformed by simple shear in a dislocation creep regime, the fast seismic direction aligns with the maximum shear direction, which is also the flow direction in the simple case of horizontal flow with a vertical velocity gradient (Zhang & Karato 1995; Karato *et al.* 2008). The anisotropy in the lower layer of the radial anisotropy models cited above can thus be interpreted as the signature of horizontal mantle flow in the asthenosphere, and the upper layer could be associated with the lithosphere. If the depth of the change in radial anisotropy is used as a proxy for the LAB, then radial anisotropy predicts an age-independent flat oceanic LAB, which cannot be due to thermal effects and appears to contradict results based on azimuthal anisotropy or 3-D isotropic velocity models.

Below the Pacific Ocean, Beghein *et al.* (2014) found that the relatively constant depth of the Gutenberg discontinuity coincides with high-vertical gradients in azimuthal anisotropy and is located within a seismic lithosphere that thickens with age. They suggested that the Gutenberg discontinuity results from dehydration of the mantle underlying the mid-ocean ridge, resulting in a chemically depleted, viscous layer that translates away from the spreading centre and becomes overprinted by lower temperatures as the plate cools down. Similarly, the quasi age-independent change in radial anisotropy at about 70 km depth could reflect different processes in the formation and evolution of oceanic plates than those seen by azimuthal anisotropy and isotropic velocities. Hier-Majumder & Drombosky (2015) explained the observed transition in radial anisotropy with calculations of melt redistribution at the base of the lithosphere. However, this does not explain the presence of azimuthal anisotropy unless the melt layers are significantly inclined from horizontal. Interestingly, Hedjazian *et al.* (2017) were able to reproduce a radial anisotropy pattern in agreement with the tomographic models without introducing any partial melt or dehydration. Using simple 2-D surface-driven mid-ocean ridge flow calculations with slow dynamic recrystallization and a mix of diffusion and dislocation creep rheology, they showed that LPO evolution results in radial anisotropy with a maximum positive gradient at a constant depth. The observed age-independent radial anisotropy signal could thus reflect the natural strain history of olivine crystals, even if the azimuthal anisotropy and velocity proxies for the LAB are thermally controlled. Similarly, with a combination of laboratory-based torsion experiments on olivine aggregates and flow modelling for a viscous fluid deforming in simple shear, Hansen *et al.* (2016) were able to predict both radial and azimuthal anisotropy patterns in agreement with the tomographic models. They obtained an age-dependent azimuthal anisotropy, consistent with thermal effects, and no age signal in the depth of the radial anisotropy change. Neither of these two last studies precludes the effect of dehydration or the presence of melt, but as pointed out by Hansen *et al.* (2016) the melt fraction should be small (<1 per cent) to not affect

Downloaded from https://academic.oup.com/gji/article-abstract/216/2/1441/5195529 by University of California, Los Angeles user on 06 February 2019

the developed anisotropy. Several researchers have additionally shown that the asthenospheric low seismic velocities found under oceans and continents can be explained by purely thermal effects without any melt requirement simply by accounting for the effect of anelasticity on wave speed (Karato & Jung 1998; Röhm *et al.* 2000; Faul & Jackson 2005; Stixrude & Lithgow-Bertelloni 2005; Goes *et al.* 2012).

Clearly, the apparent discrepancies between radial and azimuthal anisotropy models and their implications for our understanding of the origin of the LAB has gained recent attention. However, while the two types of anisotropy may be reconciled with simple flow models provided well-chosen parameters, the anisotropy models derived from regularized inversions of surface wave dispersion data are inherently non-unique, leading to the question whether the lack of age dependence in the vertical change of radial anisotropy is sufficiently resolved. Since the interpretation of tomographic models is only meaningful if the interpreted features are well resolved, it is important to determine how well constrained the shear wave velocity (V_S) and radial anisotropy (ξ) models are.

A previous study (Bartzsch *et al.* 2011) investigated how sensitive Rayleigh wave phase velocity dispersion curves are to the depth and thickness of the LAB, parametrized as a linear transition from a high-velocity lithospheric layer to a low-velocity asthenosphere. Their synthetic tests and real data applications to continental regions show that Rayleigh wave phase velocities between 22 s and 200 s have little resolution for LAB thickness, in agreement with previous work by Eaton *et al.* (2009), but can constrain transition depth quite well. However, no quantitative uncertainties were determined for any of these two variables, and the criteria to determine whether the LAB depth is well-constrained was based on an arbitrary misfit cutoff. In addition, the authors did not investigate the sensitivity of surface wave data to the LAB depth when both Love and Rayleigh waves are inverted jointly for V_S and ξ, neither did they test other LAB depth proxies such as the change in radial anisotropy with depth.

The resolution tests performed by Beghein *et al.* (2014) using the fundamental mode Love and Rayleigh waves phase velocity data of Visser *et al.* (2008a) showed that the vertical resolution of their radial anisotropy model of the Pacific upper mantle was poor. In this paper, we further explore the resolution of radial anisotropy and shear wave speed in the Pacific upper mantle using a Bayesian model space technique to determine whether the age independence of the vertical change in radial anisotropy is resolved by surface wave data. This approach enables us to explore the model space, including the null-space, and obtain quantitative uncertainties on V_S and ξ. We can define an LAB depth proxy based on V_S and one based on ξ, and from the distribution of acceptable V_S and ξ models, we can determine the distribution of possible LAB depths for each proxy. This allows us to test whether, among all the good data-fitting radial anisotropy models, there are any displaying an age dependence similar to that seen in the velocity models or whether V_S and ξ reflect different processes.

Finally, we tested the hypothesis that asthenospheric low seismic velocities may have a solid state origin and can be explained purely by thermal effects, including those on seismic attenuation, without any requirement for an additional effect of melt as advocated by several authors (Karato & Jung 1998; Röhm *et al.* 2000; Faul & Jackson 2005; Stixrude & Lithgow-Bertelloni 2005; Goes *et al.* 2012). The contribution of melt to the seismic properties of the asthenosphere has long been a matter of debate with some researchers arguing for significant melt fractions near ridges to explain low *S*-wave velocities (Forsyth *et al.* 1998; Harmon *et al.* 2009) and to explain the Gutenberg discontinuity, as discussed above (Anderson & Sammis 1970; Kawakatsu *et al.* 2009; Tharimena *et al.* 2017b), and others favouring low amounts of melt based on petrological studies (Asimow *et al.* 2004; Hirschmann 2010) or the efficiency of melt transport inferred from the decay of Ra, Pa and Th (Lundstrom 2003; Rubin *et al.* 2005; Stracke *et al.* 2006). Here we tested our models against synthetic models of seismic velocities including anelastic effects computed as in Goes *et al.* (2012) for dry and wet models. We additionally tested whether our models can discriminate between half-space (HS) and plate (PL) cooling models.

2 DATA

2.1 Surface waves

At any given point at the surface of the Earth, the measured phase and group velocity perturbation at frequency ω is the vertical average of the underlying elastic structure weighted by sensitivity kernels (Woodhouse & Dahlen 1978; Montagner & Nataf 1986):

$$\alpha_0(\omega) = \int_0^a \mathbf{K}_m(r, \omega) \mathrm{dln}\, \mathbf{m}(r) \mathrm{d}r, \tag{1}$$

where α_0 represents the measured phase or group velocity anomaly relative to its prediction by a reference model $\mathbf{m_0}$, which can be described by wave velocities, anisotropy, density and/or elastic parameters. $\ln \mathbf{m}(r) = d\mathbf{m}(r)/\mathbf{m_0}(r)$ represents relative perturbations in parameter $\mathbf{m}$ with respect to $\mathbf{m_0}$, and a stands for the radius of the Earth. $K_m(r)$ are the partial derivatives or sensitivity kernels for model parameter $\mathbf{m}$. They can be calculated for any 1-D earth model using normal mode theory (Takeuchi & Saito 1972; Rodi *et al.* 1975) and vary from mode to mode.

In this study, we tested three surface wave velocity data sets from two different groups to assess the variability of the results with the data set employed. The first data set, hereafter labelled data set 1, consisted of the isotropic part of the fundamental mode Rayleigh and Love wave global phase velocity maps obtained by Visser *et al.* (2008a), which were used by Beghein *et al.* (2014). They were obtained for 16 periods between 35 s and 175 s and resulted from the inversion of over 60 000 fundamental mode ($n = 0$) Rayleigh wave dispersion curves and over 45 000 dispersion curves for Love waves. Visser *et al.* (2008a) determined that, on average, the isotropic term of the fundamental mode phase velocity maps have a resolution comparable to that of a spherical harmonic expansion of degree order 25, yielding a lateral resolution of about 1600 km in the uppermost mantle. The second data set (data set 2) consisted of the Ekström (2011) Love and Rayleigh waves global phase velocity maps for 15 different periods between 25 s and 250 s. These maps were obtained by inversion of between 18 000 and 85 000

Downloaded from https://academic.oup.com/gji/article-abstract/216/2/1441/5195529 by University of California, Los Angeles user on 06 February 2019

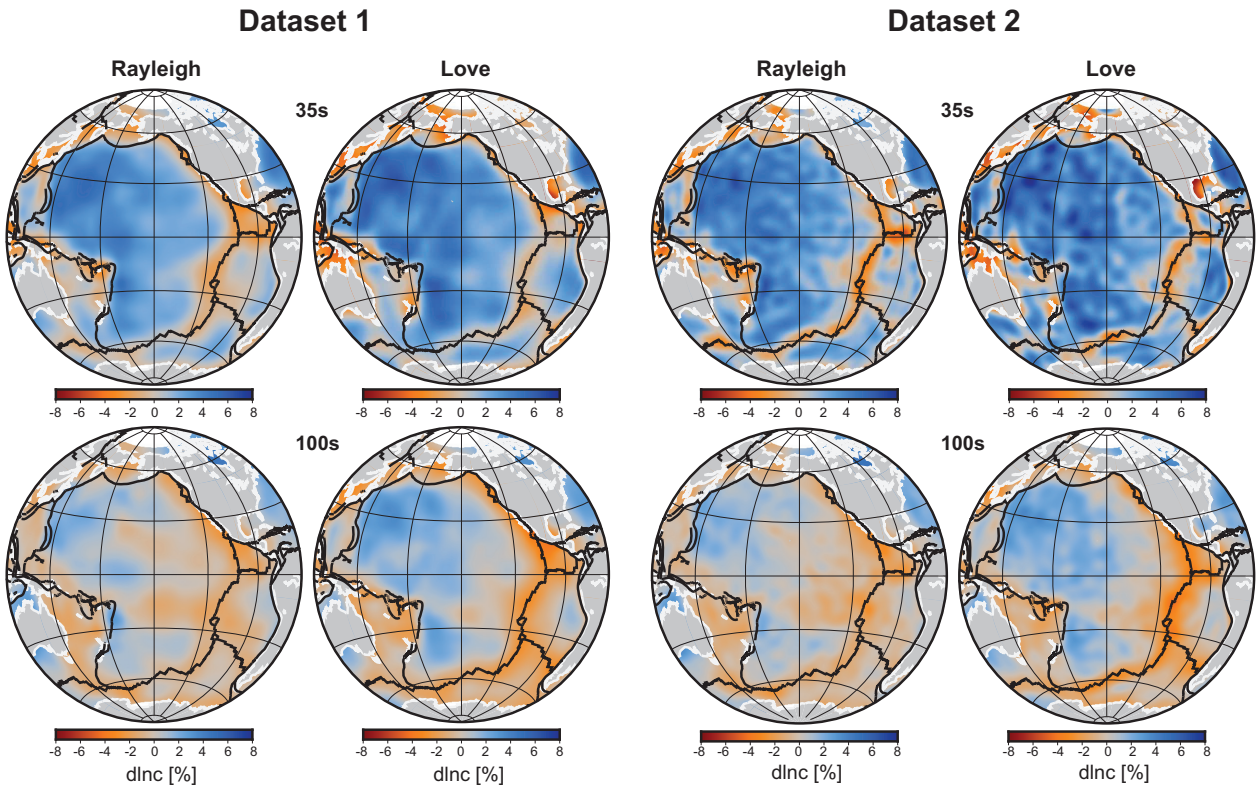

Figure 1. Love and Rayleigh waves phase velocity maps at 35s and 100s from the Visser *et al.* (2008a) data set (left-hand side) and the Ekström (2011) data set (right-hand side). Relative phase velocity perturbations are with respect to PREM (Dziewonski & Anderson 1981).

Rayleigh wave dispersion curves and between 78 000 and 286 000 Love wave dispersion curves, depending on the period. Ekström (2011) estimated that a nominal lateral resolution of 650 km was achieved in most areas. Examples of phase velocity maps for both data set 1 and data set 2 at a period of 35 s and 100 s are shown in Fig. 1. Each data set was corrected for the effects of 3-D structure in the crust using nonlinear corrections as described in Section 2.2.

Other authors have argued that crustal corrections may not be appropriate for Rayleigh wave phase velocities at periods <60s (Bozdag & Trampert 2008). Even though this issue is still being debated (Bozdag & Trampert 2008; Parisi & Ferreira 2016), we decided to account for this possibility and constructed a third data set composed of the Ekström (2011) phase velocity maps at periods > 60 s and the 25–250 s global group velocity maps obtained by the same author. The group velocity data were added to compensate the loss of sensitivity in the shallow mantle resulting from the removal of the short-period phase velocity dispersion data. Fig. 2 shows examples of those group velocity maps at 25 s and 75 s, and Fig. 3 compares sensitivity kernels for each data set. This illustrates how data set 2, with its broader frequency range, is more sensitive to structure in the uppermost 50 km than data set 1, which could yield better vertical resolution. The partial derivatives of data set 3, which is composed of the mid-to-high period phase velocity data of data set 2 and of group velocities, have larger amplitudes than the other two data sets, especially in the upper 50 km where group velocities have greater sensitivity to structure than the selected phase velocities. Table 1 summarizes the composition of those data sets.

2.2 Crustal corrections

Because surface wave velocities are highly sensitive to crustal structure and crustal thickness, it is important to account for the effect of the crust on the measurements to minimize the mapping of the crust into the mantle model (Boschi & Ekström 2002; Panning *et al.* 2010). This is especially important when modelling radial anisotropy because Love waves are sensitive to shallower structure than Rayleigh waves at the same period. Incorrectly accounting for lateral variations in crustal structure could thus affect the anisotropic mantle model (Ferreira *et al.* 2010). Full waveform tomography does not require crustal corrections, but a careful treatment of the crust is necessary to minimize crustal contamination (Lekić & Romanowicz 2011; Fichtner *et al.* 2013). Other techniques involve correcting dispersion data with predictions from a prior crustal model before inverting those data (Boschi & Ekström 2002; Kustowski *et al.* 2007; Marone & Romanowicz 2007; Ferreira *et al.* 2010; Panning *et al.* 2010) or inverting crustal thickness and/or structure jointly with mantle structure (Visser *et al.* 2008b; Chang *et al.* 2015). Alternatively, a hybrid two-step method can be employed (Burgos *et al.* 2014).

In this work we chose to calculate and apply nonlinear crustal corrections to the data using prior model crustal model CRUST1.0 (Laske *et al.* 2013). CRUST1.0 is a $1^\circ \times 1^\circ$ model in which the crust is represented as a stack of layers (ice or water, sediments and crystalline crust) with assigned thicknesses as well as *P*- and *S*-wave velocities and density. It was built using Earth's global relief model ETOPO1 (Amante

Downloaded from https://academic.oup.com/gji/article-abstract/216/2/1441/5195529 by University of California, Los Angeles user on 06 February 2019

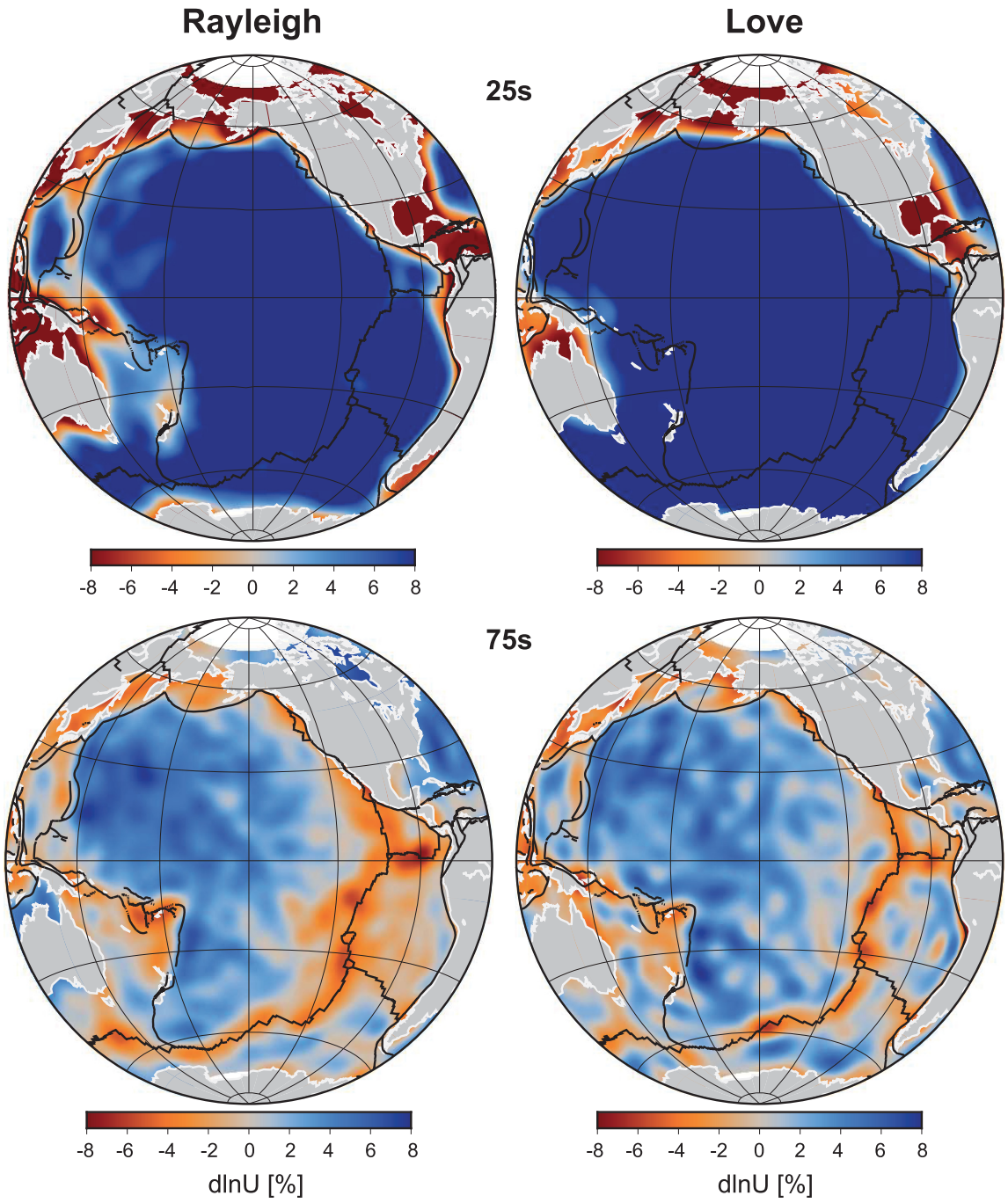

Figure 2. Love and Rayleigh waves group velocity maps at 25s and 75s from Ekström (2011). Relative group velocity perturbations are represented with respect to PREM (Dziewonski & Anderson 1981).

& Eakins 2009) for seafloor bathymetry, ice thickness and surface topography, and active source seismic data, receiver functions, and group velocity data to constrain the Moho depth and crustal velocities. Xing & Beghein (2015) showed that, for this type of correction, the choice of the crustal model does not significantly affect the resulting upper-mantle velocity or radial anisotropy model, especially in oceanic areas. They demonstrated that differences between oceanic V_S and ξ models obtained after correcting phase velocity data with different crustal models are smaller than the intrinsic uncertainties of the models due to the non-unique nature of the inverse problem.

Including the Moho depth in the parametrization, as done recently by Burgos *et al.* (2014) and Chang *et al.* (2015), can reduce the risk of mapping crustal structure into the mantle. These authors implemented such parametrization using CRUST2.0 (Bassin *et al.* 2000) as a starting crustal model. Their updated Moho depth deviated from CRUST2.0 by only ∼1–2 km in oceans. Because the model we employed in our study, CRUST1.0, was built with constraints from group velocity data with sensitivity to the crust, it is likely a more accurate seismological representation of the crust than CRUST2.0. It is also not significantly different from the updated Moho depths obtained by Burgos *et al.* (2014) or Chang *et al.* (2015) for the Pacific, especially in the light of the findings of Xing & Beghein (2015). We therefore do not believe

Downloaded from https://academic.oup.com/gji/article-abstract/216/2/1441/5195529 by University of California, Los Angeles user on 06 February 2019

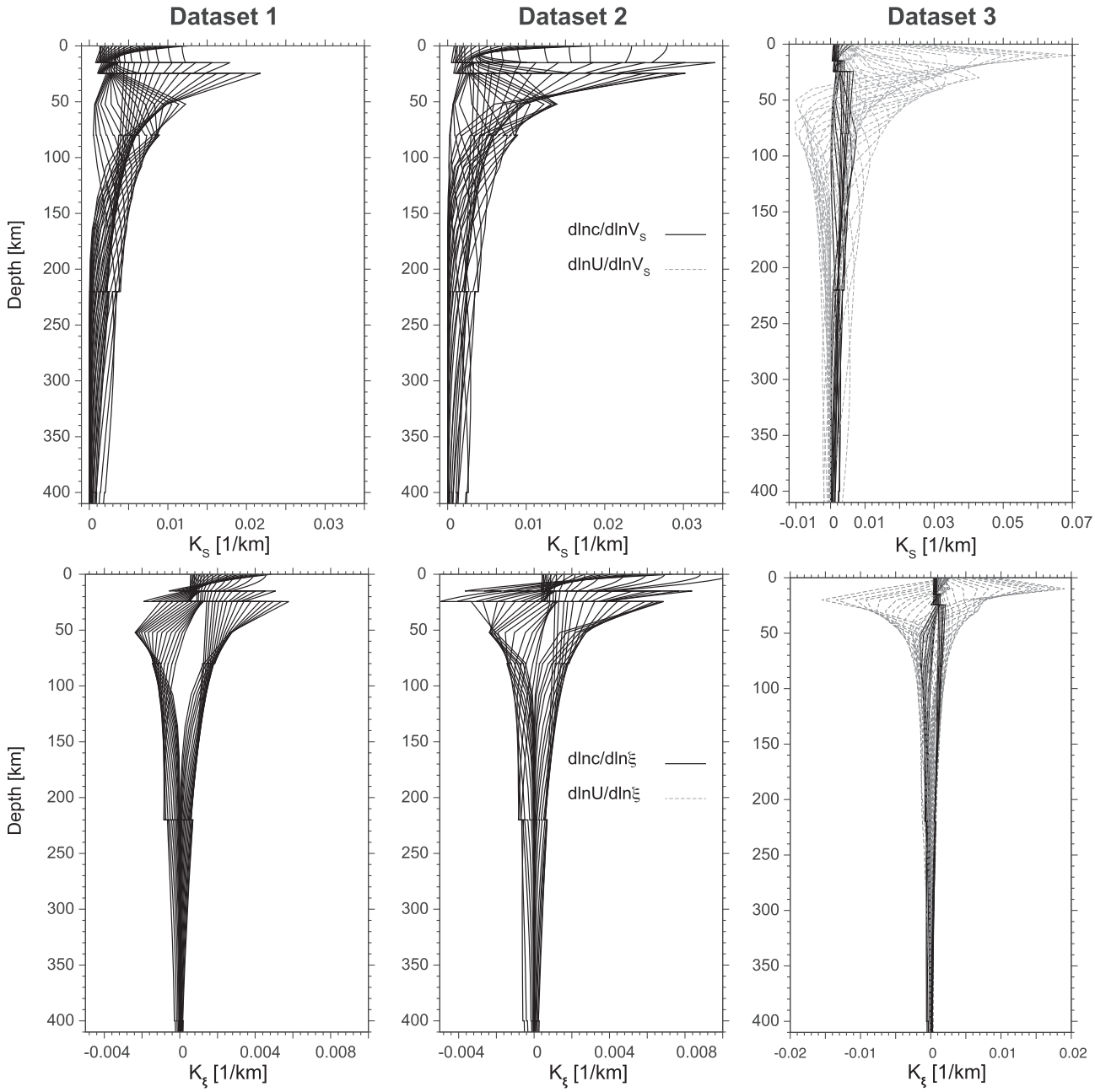

Figure 3. Sensitivity kernels for relative perturbations dV_S/V_S in shear wave velocities (top) and dξ/ξ radial anisotropy (bottom) for the three data sets described in Section 2.1. *U* and *c* stand for the group and the phase velocity, respectively. The periods at which the phase velocity kernels were calculated range from 35s and 175s for data set 1 and from 25s and 250s for data set 2. For data set 3, the periods of the phase velocity kernels range from 60s to 250s and from 25s to 250s for the group velocity kernels.

Table 1. Summary of data sets employed. *N* represents the number of periods in a data set, indices *R* or *L* stand for Rayleigh and Love waves, respectively, and *c* or *U* indicate phase or group velocities, respectively. The period range of each subset is given in the next column. N_{total} is the total number of periods for a given data set.

Data set	$N_{R,\,c}$	Period range	$N_{L,\,c}$	Period range	$N_{R,\,U}$	Period range	$N_{L,\,U}$	Period range	N_{total}
Data set 1	16	35–175 s	16	35–175 s	0	N/A	0	N/A	32
Data set 2	15	25–250 s	15	25–250 s	0	N/A	0	N/A	30
Data set 3	7	75–250 s	5	100–250 s	15	25–250 s	15	25–250 s	42

Downloaded from https://academic.oup.com/gji/article-abstract/216/2/1441/5195529 by University of California, Los Angeles user on 06 February 2019

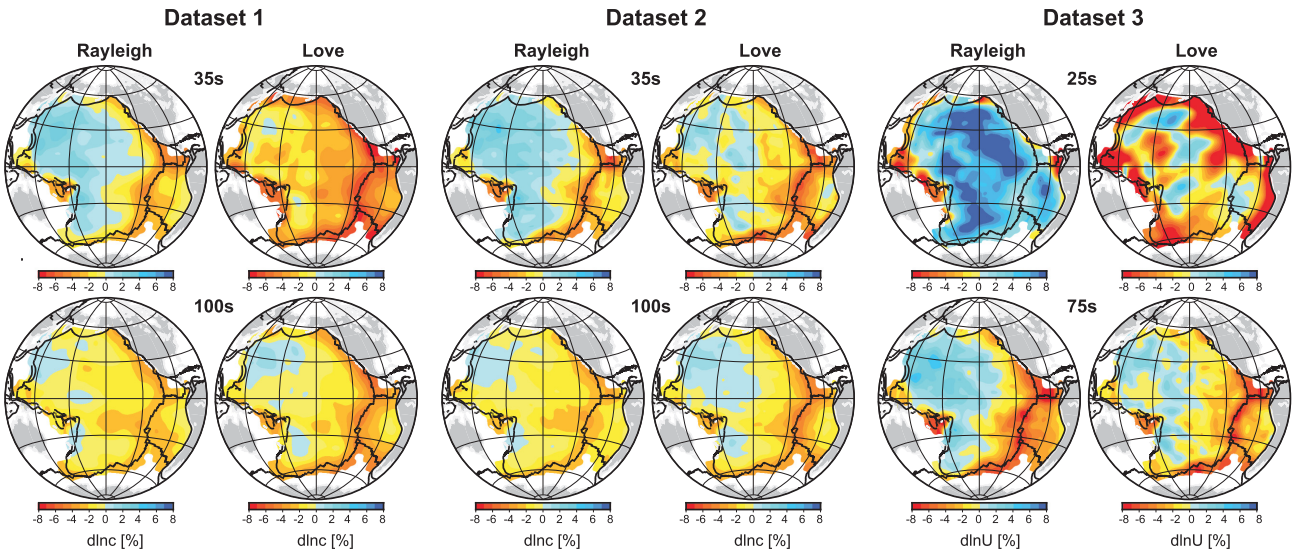

Figure 4. Examples of phase and group velocity maps corrected for the crust using CRUST1.0 (Laske *et al.* 2013) for each data set used in this study. Perturbations in phase and group velocities are with respect to PREM (Dziewonski & Anderson 1981).

that inverting jointly for crustal thickness and mantle structure would significantly affect our results, though we do think it is a crucial step to take when modelling continental areas.

We calculated nonlinear crustal corrections following a procedure similar to that of Boschi & Ekström (2002). We first constructed a 3-D reference model composed of the PREM (Dziewonski & Anderson 1981) mantle and CRUST1.0 for the crust. We divided Earth's surface into cells and used the local 1-D model at each grid cell j with computer program MINEOS (Masters *et al.* 2011) to calculate local, theoretical phase c_j and group velocities U_j and local eigenfunctions, which were then used to determine local sensitivity kernels $K_{m,j}$, where m represents a model parameter. At each grid cell j, the difference between the phase c_j or group velocity U_j predicted by the 3-D model and that calculated from PREM (c_0 or U_0) is the contribution of the crustal model to the measured velocity perturbation $\mathrm{d}c_{c,j}$ or $\mathrm{d}U_{c,j}$, that is, it is the crustal correction. After removing this correction from the measured phase or group velocity anomaly, we are left with a corrected signal $(\frac{\mathrm{d}c_c}{c})_j$ or $(\frac{\mathrm{d}U_c}{c})_j$ that represents the phase or group velocity anomaly due to a local mantle perturbation with respect to the reference model at grid cell j. This remaining signal can thus be inverted to infer local perturbations in mantle structure with respect to PREM using the local sensitivity kernels:

$$\left(\frac{\mathrm{d}c_c}{c}\right)_j = \int_0^{Moho} \sum_i \left[K_{m_{i,j}}(r)\mathrm{d}\ln m_{i,j}(r)\right] \mathrm{d}r, \tag{2}$$

where the sum over i is carried out over all model parameters. A similar equation applies to group velocities. Note that this method is only strictly valid if there is no mode coupling since it assumes that the effect of crustal structure can be computed independently at each location on the Earth's surface. Examples of the corrected phase and group velocity maps are shown in Fig. 4 and comparison with Figs 1 and 2 demonstrates that the crust contributes significantly to the measurements.

3 METHOD

3.1 Forward problem and parametrization

As shown by eq. (1), the measured phase and group velocity perturbations are weighted depth averages of the underlying structure, and the dispersive properties of surface waves imply that the shorter periods are more sensitive to the shallower structure (Fig. 3). We note that, as opposed to mode-based waveform inversion techniques, an implicit assumption in eq. (1) is that there is no mode coupling. This is clearly an approximation since we know that lateral heterogeneities and anisotropy can cause coupling between modes (e.g. Park & Yu 1992; Beghein *et al.* 2008), but its effects are poorly known.

In an isotropic medium, the model parameters are density ρ and two elastic coefficients: the Lamé parameter λ and the shear modulus μ, or alternatively the bulk modulus κ and the shear modulus. Eq. (1) becomes

$$\alpha_0(\omega) = \int_0^a \left[K_\rho(r,\omega)\mathrm{dln}\,\rho(r) + K_\mu(r,\omega)\mathrm{dln}\,\mu(r) + K_\kappa(r,\omega)\mathrm{dln}\,\kappa(r)\right]\mathrm{d}r. \tag{3}$$

In a general anisotropic medium, a total number of 21 independent parameters are needed to fully describe the fourth-order elastic stiffness tensor. Because seismic data cannot resolve all 21 parameters, we make assumptions regarding the symmetry of the anisotropic medium to reduce the number of unknowns. In the simple case of radial anisotropy, the medium has hexagonal symmetry with a vertical symmetry axis

Downloaded from https://academic.oup.com/gji/article-abstract/216/2/1441/5195529 by University of California, Los Angeles user on 06 February 2019

and can be described by five independent parameters: the velocity of vertically polarized shear waves V_{SV}, of horizontally polarized shear waves V_{SH}, of vertically and horizontally propagating P-waves V_{PV} and V_{PH}, respectively, and parameter η which describes wave propagation at an intermediate angle:

$$\alpha_0(\omega) = \int_0^a \left[K_{V_{PV}}(r,\omega)\mathrm{dln}\, V_{PV}(r) + K_{V_{PH}}(r,\omega)\mathrm{dln}\, V_{PH}(r) + K_{V_{SV}}(r,\omega)\mathrm{d}\ln V_{SV}(r) + K_{V_{SH}}(r,\omega)\mathrm{d}\ln V_{SH}(r) + K_\eta(r,\omega)\mathrm{d}\ln\eta(r) + K_\rho(r,\omega)\mathrm{d}\ln\rho(r)\right]\mathrm{d}r. \quad (4)$$

A parametrization in terms of the Love elastic parameters A, C, N, L and F (Love 1927) is sometimes employed (Beghein 2010; Chang *et al.* 2014), with $A = \rho V_{PH}^2$, $C = \rho V_{PV}^2$, $N = \rho V_{SH}^2$, $L = \rho V_{SV}^2$, $F = (A - 2L)\eta$. Here, we chose instead to follow Panning & Romanowicz (2006) and used another equivalent parametrization:

$$V_P^2 = (V_{PV}^2 + 4V_{PH}^2)/5 \quad (5)$$

$$V_S^2 = (2V_{SV}^2 + V_{SH}^2)/3 \quad (6)$$

$$\phi = V_{PV}^2/V_{PH}^2 \quad (7)$$

$$\xi = V_{SH}^2/V_{SV}^2 \quad (8)$$

$$\eta = F/(A - 2L), \quad (9)$$

where V_P and V_S are Voigt average isotropic velocities representing upper bounds on the effective elastic moduli (Babuška & Cara 1991). ϕ and ξ represent P-wave and S-wave radial anisotropy, respectively. This parametrization enables us to directly invert for anisotropy instead of calculating *a posteriori* from separate inversions of V_{SV} and V_{SH}, which can cause unwanted roughness in the mapped anisotropic structure (Nettles & Dziewoński 2008). Eq. (1) therefore becomes

$${}_k\alpha_0 = \int_0^a \left[{}_kK_{V_P}(r)\mathrm{dln}V_P(r) + {}_kK_{V_S}(r)\mathrm{dln}V_S(r) + {}_kK_\phi(r)\mathrm{d}\ln\phi(r) + {}_kK_\xi(r)\mathrm{d}\ln\xi(r) + {}_kK_\eta(r)\mathrm{d}\ln\eta(r) + {}_kK_\rho(r)\mathrm{d}\ln\rho(r)\right]\mathrm{d}r, \quad (10)$$

where k represents the mode considered and ω is omitted for clarity. Partial derivatives were calculated using Fortran program MINEOS (Masters *et al.* 2011). Not all of these six parameters are, however, well resolved by surface waves because of reduced sensitivity to V_P, ϕ, η and ρ and because of parameter trade-offs. For this reason, we used the empirical relationships established by Montagner & Anderson (1989) from petrological considerations to scale perturbations in compressional wave velocity and density to changes in shear wave velocity, and to scale changes in compressional wave anisotropy and in η to perturbations in shear wave anisotropy:

$$\frac{\mathrm{d}\ln V_P}{\mathrm{d}\ln V_S} = 0.5 \quad (11)$$

$$\frac{\mathrm{d}\ln\rho}{\mathrm{d}\ln V_S} = 0.33 \quad (12)$$

$$\frac{\mathrm{d}\ln\phi}{\mathrm{d}\ln\xi} = -2.5 \quad (13)$$

$$\frac{\mathrm{d}\ln\eta}{\mathrm{d}\ln\xi} = -1.5. \quad (14)$$

Such scaling factors between density and velocities imply that thermal effects are dominant, but it should be noted that thermal and plausible chemical mechanisms (melt-depletion, eclogite enrichment) span a strongly overlapping range at lithosphere–asthenosphere depths. Furthermore, surface wave propagation is not very sensitive to V_P and density, so somewhat different scaling or not using any scaling at all is not expected to affect results, except for a possible increase in model uncertainties if no scaling were used (Beghein 2010).

We parametrized the Earth horizontally by dividing its surface into $5^\circ \times 5^\circ$ cells, and conducted the inversions of eq. (10) for each cell separately. At every grid cell, we used a depth parametrization for $\mathrm{dln}\, V_S(r)$ and $\mathrm{dln}\,\xi(r)$ composed of $M = 8$ cubic spline function $S_i(r)$ (i=1,...,M) for data sets 1 and 2, and $M = 9$ splines for data set 3 because of the increased sensitivity at shallow depths (Fig. 5):

$$\mathrm{dln}V_S(r) = \sum_{i=1}^{M} \mathrm{dln}V_S^i S_i(r) \quad (15)$$

Downloaded from https://academic.oup.com/gji/article-abstract/216/2/1441/5195529 by University of California, Los Angeles user on 06 February 2019

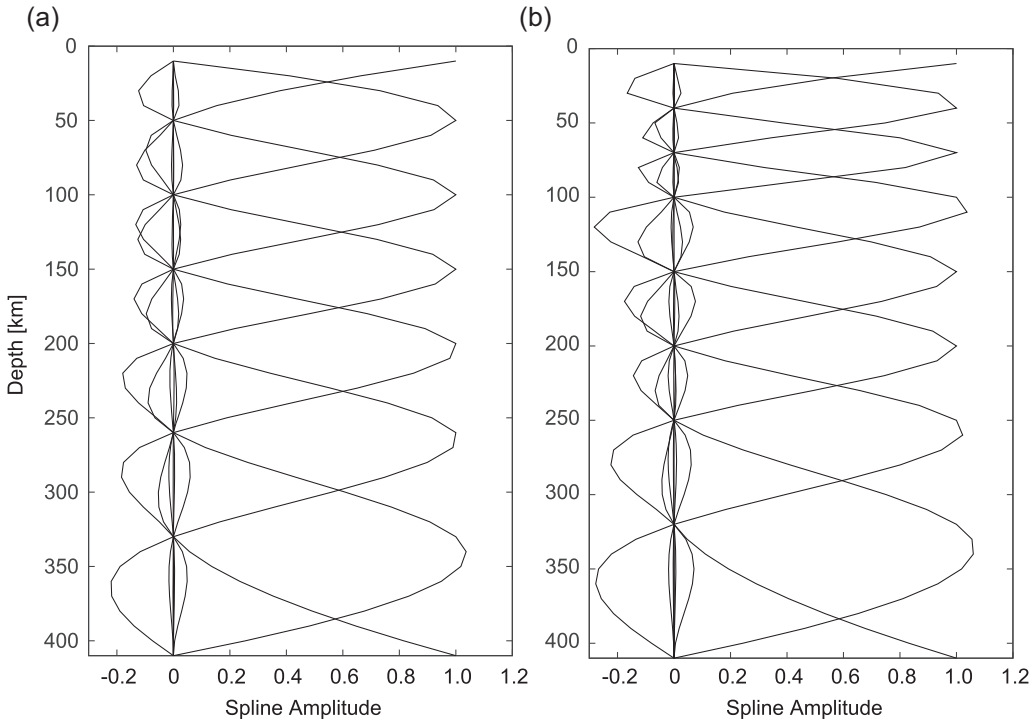

Figure 5. Cubic spline functions employed to parametrize vertically the model parameters in the inversions of data set 1 and data set 2 (left-hand panel) and of data set 3 (right-hand panel).

$$\mathrm{d}\ln\xi(r) = \sum_{i=1}^{M} \mathrm{d}\ln\xi^i S_i(r), \tag{16}$$

where $\mathrm{dln}V_S^i$ and $\mathrm{dln}\,\xi^i$ are the coefficients of the ith spline. Note that, since the top of the splines is defined by the local Moho and not Earth's surface, the spline functions are varying laterally. The vertical spacing between the splines is also variable to reflect changes in the depth sensitivity of the data. Eq. (10) can be written as:

$$\mathbf{Gm} = \mathbf{d}, \tag{17}$$

where vector **d** represents the data vector, and **m** is the vector containing the model parameters, that is, the $\mathrm{dln}V_S^i$ and $\mathrm{dln}\,\xi^i$ of eqs (15) and (16). Matrix **G** is the kernel matrix and its elements G_{ki} can be calculated using the prior constraints of eqs (11)–(14) and by integrating the sensitivity kernels projected onto the spline functions $S_i(r)$

$$G_{ki} = \int_0^a \left[{}_kK_{V_S}(r) + 0.5\,{}_kK_{V_P}(r) + 0.33\,{}_kK_{\rho}(r) + {}_kK_{\xi}(r) - 2.5\,{}_kK_{\phi}(r) - 1.5\,{}_kK_{\eta}(r)\right] S_i(r)\mathrm{d}r. \tag{18}$$

At each grid cell, we have 16 model parameters for data sets 1 and 2 and 18 for data set 3. And the models at each grid cell are constrained by 32 data points (16 Rayleigh and 16 Love wave phase velocities) for data set 1, by 30 data points for data set 2 (15 Rayleigh and 15 Love wave phase velocities) and by 42 data points for data set 3 (i.e. 7 Rayleigh and 5 Love wave phase velocities, as well as 15 Rayleigh and 15 Love group velocities). Matrix **G** has thus 32 rows and 16 columns for data set 1, 30 rows and 16 columns for data set 2, and 42 rows and 18 columns for data set 3.

3.2 Modelling

Regularized inversions do not always provide reliable quantitative model uncertainties, especially in the presence of a large null space (Trampert 1998). An alternative approach can be found in direct search techniques. Without needing to implicitly introduce strong *a priori* information, this type of method is able to explore the model space, including null-space, giving us a better description of the range of possible models instead of just one 'best'. Here we utilized a two-part global optimization technique, namely the Neighbourhood Algorithm (NA) (Sambridge 1999a,b).

The first part of NA is a direct search of the model space. First, a number of samples are randomly generated in the model space and the model space is divided into Voronoi cells using this initial sampling. Each cell is centred on one of the models by construction. An approximate misfit surface is determined by calculating the misfit of each of these models. At each subsequent iteration, n_s new samples are

Downloaded from https://academic.oup.com/gji/article-abstract/216/2/1441/5195529 by University of California, Los Angeles user on 06 February 2019

then generated by performing a uniform random walk with a Gibbs sampler in the Voronoi cell of each of the n_r best-fitting models. The Voronoi cells are updated to accommodate the newly generated models, and misfits are calculated for those new models, determining a new misfit surface. Misfits are then ranked among all the existing models to determine the next set of n_r best-fitting models. At each iteration, the sampling density therefore increases in the neighbourhoods of the better data-fitting models, and the NA is able to use the information contained in the previous models to adapt the sampling. The choice of the tuning parameters n_r and n_s is generally decided by trial and error to control the convergence speed and the sampling quality. A small n_s/n_r ratio implies a slower convergence of the algorithm but helps perform a sampling of the model space as thorough as possible to avoid getting trapped in a local minimum. The iteration is stopped by the user when the misfit does not show any clear decrease with each iteration. While we agree that one can never be certain to have fully sampled the model space, we did perform a large number of tests until we decided we satisfactorily sample the model space and insure stability and convergence of the results. We settled on $n_s = n_r = 10$ and ran 20 000 iterations. Fig. S1 of the Supporting Information displays how the misfit varies with the number of models generated for the different model parameters inverted at a grid cell located at -15° latitude and 220° longitude. In this figure, we also compare the results for the chosen tuning parameters (Fig. S1A, Supporting Information) with results obtained from a broader model space search with $n_s = n_r = 20$ (Fig. S1B, Supporting Information) to demonstrate that the ensemble of solutions obtained was stable and had converged.

In this work, we first carried out regularized inversions of the surface wave data using eq. (17) and the singular value decomposition (SVD) method of Matsu'ura & Hirata (1982). This technique is described in detail in Yuan & Beghein (2014). We then ran the first part of the NA using a uniform prior model distribution around the results of the regularized inversion: each of the 16 model parameters were allowed to vary by 5 per cent with respect to the local reference model and around the inversion results. Searching the model space around the inversion results has the advantage of accelerating the sampling convergence if the model distribution is close to a Gaussian while still allowing the NA to find good data fitting models away from the inversion results. We compared our results with those resulting from a model space search around zero and showed they are equivalent (see Section 4).

In the second part of the NA, a Bayesian appraisal of the ensemble of models obtained from sampling the model space is performed. Unlike other statistical techniques, such as importance sampling, which draws inferences on the models using only a subset of the ensemble of models generated, the NA makes use of all the models, good and bad, generated during the first stage. The low and high misfits of the models are converted to high and low likelihoods, respectively. Assuming Gaussian-distributed errors on the measurements, the likelihood function is defined as

$$P(\mathbf{d}|\mathbf{m}) = \exp\left[-\frac{1}{2}(\mathbf{d}-\mathbf{g}(\mathbf{m}))^T \mathbf{C}_\mathrm{D}{}^{-1}(\mathbf{d}-\mathbf{g}(\mathbf{m}))\right], \tag{19}$$

where $\mathbf{g}(\mathbf{m})$ are phase velocity predictions calculated from model $\mathbf{m}$ and eq. (17), and $\mathbf{C}_\mathrm{D}$ is the data covariance matrix. Here, the data covariance matrix is a diagonal matrix whose elements are given by the data variance. For data set 1, the data variance was provided by Visser *et al.* (2008a) for each fundamental and higher mode. Because data sets 2 and 3 were not provided with uncertainties, we applied the same relative uncertainties as those determined by Visser *et al.* (2008a) to the Ekström (2011) phase velocities. For the group velocities, we imposed relative uncertainties twice as large as for the phase velocities as these data have typically larger error bars than phase velocities (Dr. Zhitu Ma, personal communication, 2017).

The likelihood function $P(\mathbf{d}|\mathbf{m})$ is then used to obtain the posterior probability density functions (PPDFs) given by Bayes' theorem (Bayes & Price 1763):

$$P(\mathbf{m}|\mathbf{d}) \propto \rho(\mathbf{m})P(\mathbf{d}|\mathbf{m}), \tag{20}$$

where $P(\mathbf{m}|\mathbf{d})$ is a likelihood function representing the fit to the data, and $\rho(\mathbf{m})$ is the prior probability density distribution, defined here as uniform distributions around the inversion results. These PPDFs can be used to assess the robustness of the model parameters as they can be used to calculate the mean values and uncertainties of the model parameters, as well as covariance matrix and resolution matrix.

For a PPDF $P(\mathbf{m}|\mathbf{d})$, the posterior mean model for the ith parameter is given by the following integral performed over the model space (Sambridge 1999b):

$$< m_i >= \int m_i P(\mathbf{m}|\mathbf{d})\mathrm{d}\mathbf{m}. \tag{21}$$

The posterior variances of the model parameters can be obtained from the diagonals of the posterior model covariance matrix defined by

$$C_{i,j} = \int m_i m_j P(\mathbf{m}|\mathbf{d})\mathrm{d}(\mathbf{m}) - < m_i >< m_j > . \tag{22}$$

Note that the concepts of covariance matrix and the resolution kernels are linearized concepts, and are most useful if the PPDF has a single dominant peak, for example, if the distribution is Gaussian. They are used here to get quantitative uncertainties on the model parameters, but one should keep in mind the limitations of these definitions. Because the null-space is included in the model space sampling, the model uncertainties inferred are more accurate than those resulting from regularized inversions that tend to underestimate posterior variance, especially in the presence of a large model null-space (Trampert 1998; Beghein & Trampert 2003; Beghein 2010).

Downloaded from https://academic.oup.com/gji/article-abstract/216/2/1441/5195529 by University of California, Los Angeles user on 06 February 2019

The 1-D marginal distribution of a given model parameter m_i can be obtained by integrating $P(\mathbf{m}|\mathbf{d})$ numerically over all other parameters (Sambridge 1999b):

$$M(m_i) = \int \dots \int P(\mathbf{m}|\mathbf{d}) \prod_{k=1,k\neq i}^{d} \mathrm{d}m_k, \tag{23}$$

where d is the total number of model parameters. The shape and width of these 1-D marginals provide useful information on how well constrained a given parameter is and whether the model distribution is Gaussian, in which case the mean $<m_i>$ coincides with the peak of the distribution, that is, the most likely value. In our study, they can also be used to calculate the distribution of possible LAB depths at a given grid cell, thereby providing quantitative uncertainties for each proxy employed. Fig. S2 of the Supporting Information shows an example of PPDFs for the grid cell located at -15° latitude and 220° longitude. The posterior distributions of the best-resolved parameters display clear peaks (e.g. the second V_S spline parameter) while parameters that are less well constrained have broader PPDFs with less well-defined peaks (e.g. the sixth V_S spline parameter). We note that because some of the PPDFs peak towards the edges of the model space, one might be tempted to expand the model space boundaries to better locate these peaks. However, changing the model space boundary for one parameter can affect the most likely value of another parameter if the two parameters trade-off strongly with one another (Beghein 2010). In addition, it is necessary to remain within the framework of perturbation theory, which prevents us from searching too wide of a model space.

4 RESULTS

4.1 Tomographic models from regularized inversions

In the following section, Model1_SVD, Model2_SVD and Model3_SVD refer to the velocity and radial anisotropy models derived from the regularized inversion of data set 1, data set 2, and data set 3, respectively.

For all models, the number of independent parameters was six as determined by our SVD method (Matsu'ura & Hirata 1982). The achieved variance reduction averaged over the study area was 98.6 per cent for Model1_SVD, 95 per cent for Model2_SVD and 79 per cent for Model3_SVD. For Model3_SVD, we calculated that the phase velocities were better explained (at 86 per cent variance reduction) than the group velocities (with a variance reduction of 58 per cent). However, with simple F-tests (Menke 2012) we determined that the difference between the variance reduction of data set 2 and that of data set 3, as well as the difference in variance reduction between the group and the phase velocities of data set 3, are likely not significant at the 95 per cent confidence level.

Synthetic tests showing the vertical resolution achieved with each data set and the chosen regularization are represented in Figs S3–S5 (Supporting Information). The depth resolution of data sets 1 and 2 for V_S is between 50 and 70 km in the upper 150–200 km, and closer to 30 km for data set 3. Neither data set 1 nor data set 2 performs particularly well for radial anisotropy. Data set 3, however, should be able to recover an upper radial anisotropy layer of about 80 km. These tests suggest that the inclusion of group velocity data helps improve the depth resolution of the models, but that, whether we use V_S or ξ to estimate LAB depths, we should not be confident about LAB depth less than 50 km.

The V_S models (Fig. 6) are overall consistent with one another and with previously published models, despite some differences between model amplitudes, which are likely due to differences in regularizations and in the phase velocity maps, which themselves result from a regularized inversion of path-averaged dispersion measurements. The inclusion of group velocity data did not affect the models significantly, although some differences are visible. For all models, we observe that mid-ocean ridges are characterized by relatively low velocities at shallow depths whereas the rest of the region displays higher velocities than average. As depth increases, the relatively low V_S becomes more widespread below the Pacific ocean, and the faster-than-average velocities that are likely the signature of a cool lithosphere disappear between 100 and 150 km. The difference between the area covered by positive velocity anomalies at 100 km depth in Model1_SVD and that of Model2_SVD or Model3_SVD suggests that the Ekström (2011) data set favours a shallower high-velocity lid than the Visser *et al.* (2008a) data set.

While the velocity models are in general agreement with one another, the radial anisotropy models obtained exhibit significant discrepancies. Fig. 7 displays maps of relative perturbations $\mathrm{d}\ln\xi$ in radial anisotropy (with $\xi = V_{SH}^2/V_{SV}^2$) with respect to anisotropic PREM at different depths. In PREM, the upper 220 km of the mantle are characterized by $V_{SH} > V_{SV}$ ($\xi < 0$) and $V_{SH} = V_{SV}$ ($\xi = 1$) at greater depths. Therefore, in our models $\mathrm{d}\ln\xi < 0$ corresponds an even stronger $V_{SH} > V_{SV}$ signal than in PREM, and $\mathrm{d}\ln\xi > 0$ means the total radial anisotropy ξ is less strongly negative than in PREM. Locations with very large $\mathrm{d}\ln\xi > 0$ anomalies may even correspond to $V_{SV} > V_{SH}$. Fig. 7 shows that $\mathrm{d}\ln\xi < 0$ in the top 100 km and relatively uniformly across the Pacific for Model1_SVD, with decreasing amplitude as depth increases. We observe more lateral variations of ξ in Model2_SVD, with more positive anomalies at 80 and 100 km depth than in Model1_SVD. In both models, the strongest anomalies are negative. Model3_SVD has a strikingly different radial anisotropy signal than the other two models as it is negative only in the top 50 km and becomes positive over most of the study area at 80 km depth. These differences between models already suggest that the interpretation of existing radial anisotropy models in terms of the LAB is non-unique.

Downloaded from https://academic.oup.com/gji/article-abstract/216/2/1441/5195529 by University of California, Los Angeles user on 06 February 2019

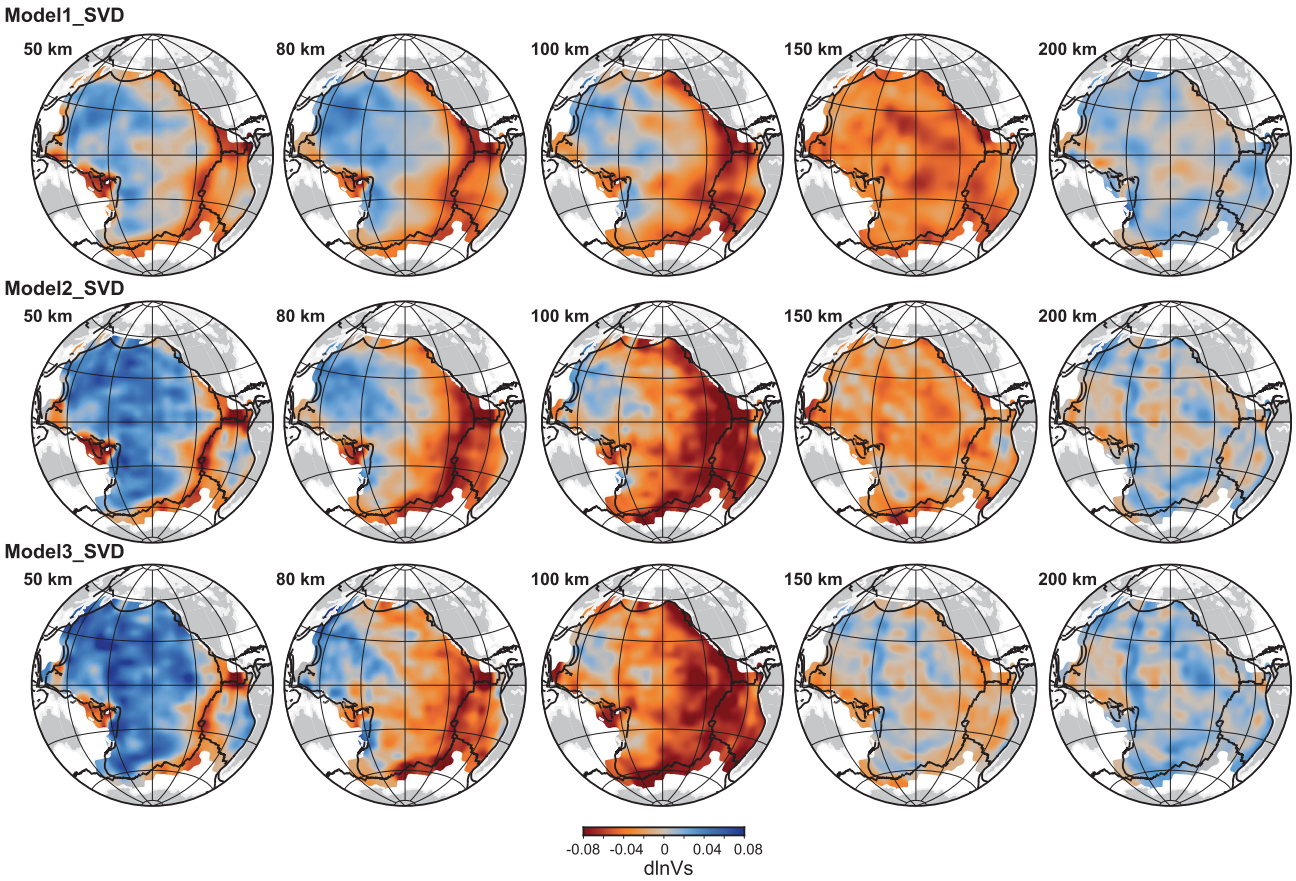

Figure 6. Maps of relative shear wave velocity perturbations at different depths in the uppermost mantle. They were obtained from the regularized inversion of data set 1 (top), data set 2 (middle) and data set 3 (bottom). Perturbations in V_S are with respect to CRUST1.0 (Laske *et al.* 2013) superimposed onto anisotropic PREM (Dziewonski & Anderson 1981).

4.2 Tomographic models from the model space search

The application of the NA to each data set yielded new distributions of tomographic models. With this approach, each model parameter is described by a PPDF instead of obtaining a single model for each data set based on implicit regularization. The model space search was centred around the models obtained by SVD. The prior was a uniform distribution between −0.05 and 0.05 around the SVD results at all depths. For instance, if the *i*th spline coefficient $d\ln V_S^i$ (Eq. 15) of the SVD model has a value of 0.04, the prior distribution for this parameter is uniform between −0.01 and 0.09. Similarly, if the *i*th radial anisotropy spline coefficient $d\xi^i$ has a value of 0.05 in the SVD model, the model space search for this parameter ranges from 0 to 0.1.

Figs 8 and 9 represent the V_S and ξ mean models and their uncertainties. The mean models (labelled Model1_m, Model2_m and Model3_m) and the uncertainty maps were constructed at each grid cell using the weighted mean and standard deviation of the PPDFs representing the $d\ln V_S^i$ and $d\ln \xi^i$ spline coefficients (Eq. 16). For both parameters, the uncertainties are displayed as absolute values, that is, a mean value of 0.04 in $d\ln \xi$ and an uncertainty of 0.03, for instance, means $d\ln \xi = 0.04 \pm 0.03$ (and similarly for $d\ln V_S$). The variance reduction of the mean models were very close to that of the SVD inversion results for data set 1 and data set 2, with values of 98.5 and 95.5 per cent, respectively. For data set 3, the mean model had an improved misfit compared to the SVD results with 85.7 per cent of the data explained, as opposed to 79 per cent for Model3_SVD. Importantly, we remind the reader that when comparing variance reduction between the two methods, it is essential to remember that the mean model obtained by NA is not necessarily one of the best data fitting models as they coincide only when the PPDFs are Gaussian, and it is not always the case here. The misfit values reported here therefore show that the NA was successful at finding models that explained the data better than the regularized inversions.

The mean velocity models strongly resemble their regularized counterparts, except for Model2_m at 200 km depth that displays stronger amplitudes than Model2_SVD. Model3_m has slightly more negative velocity perturbations at 200 km than Model3_SVD. The average uncertainties are around 0.03 for $d\ln V_S$ in both Model1_m and Model2_m, and about 0.02 for Model3_m. The mean anisotropy models are also close to the anisotropy models obtained by regularized inversions, the strongest differences being for data set 2 at 100 km depth where Model2_m has more positive anomalies than Model2_SVD. In addition, the anisotropy anomalies of Model3_m at and below 80 km depth are slightly stronger than those of Model3_SVD. In Model2_m, while the pattern of anisotropy at 50 and 80 km depth are similar and display mostly negative anomalies of decreasing amplitude with depth, the pattern of anisotropy shows mostly positive perturbations and identical

Downloaded from https://academic.oup.com/gji/article-abstract/216/2/1441/5195529 by University of California, Los Angeles user on 06 February 2019

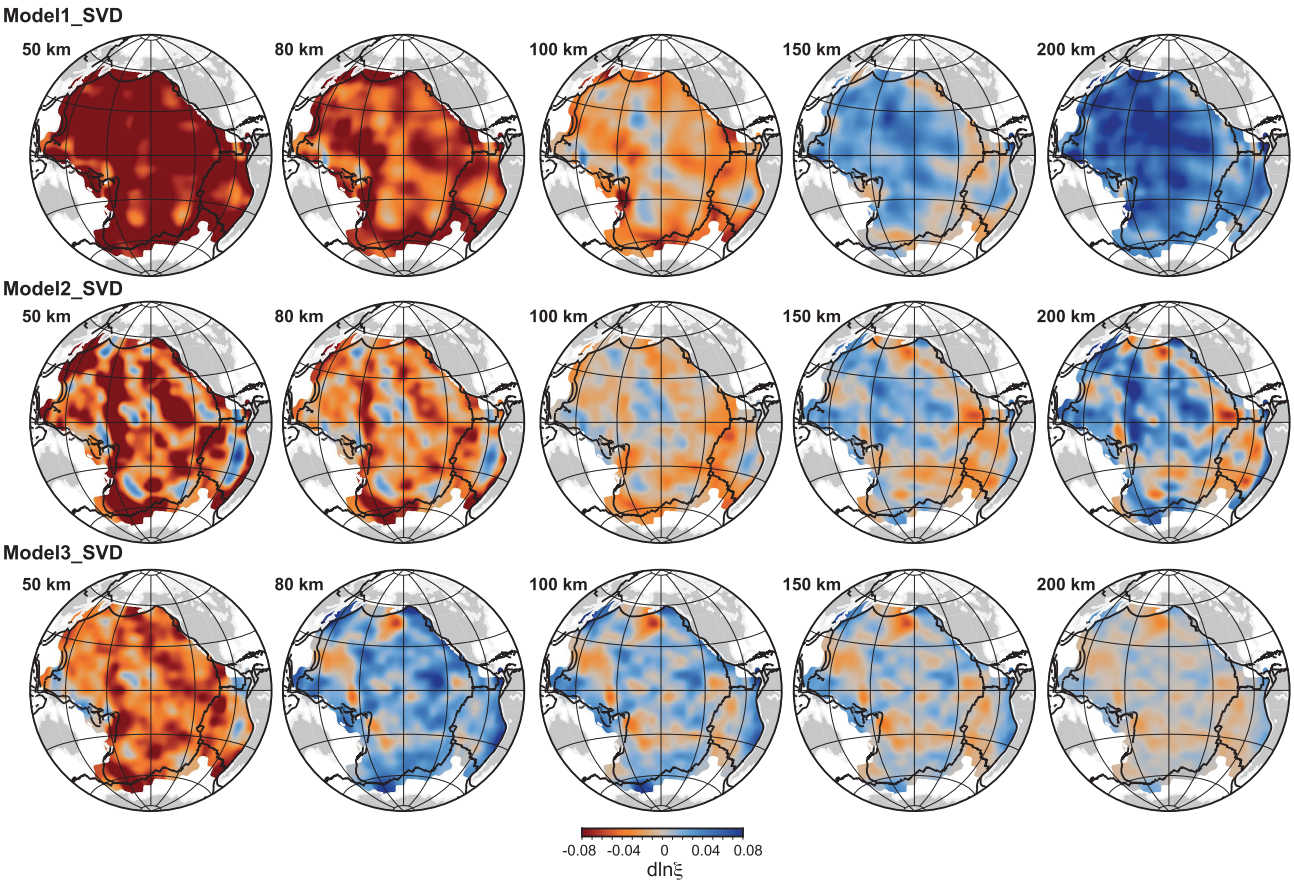

Figure 7. Maps of relative perturbations in shear wave radial anisotropy at different depths in the uppermost mantle. They were obtained from the regularized inversion of data set 1 (top) and data set 2 (middle) and data set 3 (bottom). Perturbations in ξ are with respect to CRUST1.0 (Laske *et al.* 2013) superimposed onto anisotropic PREM (Dziewonski & Anderson 1981).

patterns at 100, 150 and 200 km depth. In Model3_m, just like in Model3_SVD, there is a clear change from $\mathrm{d}ln\xi < 0$ at 50 km and $\mathrm{d}ln\xi > 0$ below. The average uncertainties are generally smaller than the mean values in all models.

We also ran the NA around model PREM (Fig. S6, Supporting Information) using data set 1 as a test case to insure the results of Figs 8 and 9 did not represent a local minimum, biased towards the SVD model. These additional model space searches were slower to converge than those centred around the regularized inversion results, as expected when sampling a wider model space. The new models show slightly stronger amplitudes than those of Model1_m and some more lateral variations, but also larger uncertainties. This implies that the difference between models obtained by searching the model space around PREM or around the SVD model are likely not significant.

4.3 LAB depth proxies and uncertainties

As discussed in Section 1, several different seismological proxies can be used to characterize the LAB and determine its depth. Here, we focus on two proxies, one based on the *S*-wave velocity models and one based on the radial anisotropy models. The 'seismic' LAB can be related to the change in velocity between a high-velocity lithosphere and a low-velocity asthenosphere. In previous studies, some authors chose to use the depth of the maximum negative velocity gradient (maximum of $-\partial V_S/\partial z$) to map the LAB depth (Burgos *et al.* 2014). Others (Bartzsch *et al.* 2011) defined the seismic LAB depth as the middle of the interval over which V_S decreases since this drop may be sharp (over a few kilometres) or gradual (a few tens of kilometres). Here, we chose to employ the same proxy as Bartzsch *et al.* (2011). In addition, because the classical plate tectonics definition of the LAB is that it corresponds to a change in mechanical response, the LAB may be expected to be associated with a change in radial anisotropy similar to what has been found in azimuthal anisotropy models (e.g. Beghein *et al.* 2014). We thus employed the depth of the largest positive ξ gradient ($\partial\xi/\partial z$) as another proxy for the LAB depth as in Burgos *et al.* (2014). We first calculated these proxies for each inverted data set and at each grid cell using the V_S and ξ profiles obtained from our regularized inversions. We plotted them in map view (Fig. 10) and as a function of oceanic crust age (Fig. 11). The error bars displayed in Fig. 11 represent the range of values obtained across the study area for a given age but do not account for the non-uniqueness of the inverse problem.

With the V_S-defined LAB proxy, Model1_SVD yields a shallow LAB depth of ∼40 km at the East Pacific Rise (EPR) and the Cocos–Nazca spreading ridge, which deepens rapidly with age to a depth of ∼120 km over much of the Pacific (Fig. 10). The change in LAB depth with crustal age is also visible in Model2_SVD, but more gradual than in Model1_SVD, also starting at depths of around 40 km near the

Downloaded from https://academic.oup.com/gji/article-abstract/216/2/1441/5195529 by University of California, Los Angeles user on 06 February 2019

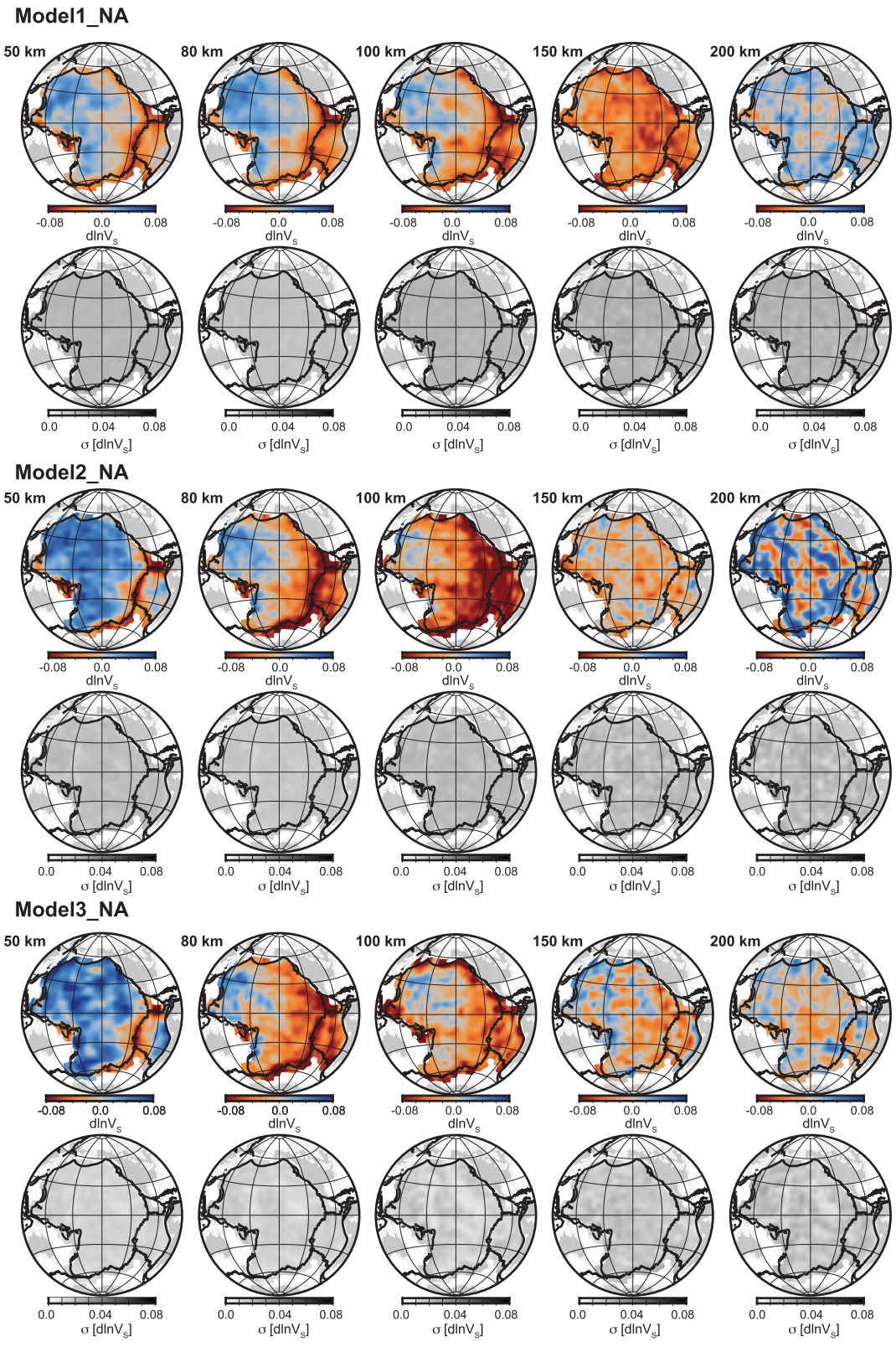

Figure 8. Mean velocity models and standard deviation obtained by applying the NA to data set 1 (top) and data set 2 (middle), and data set 3 (bottom).

Downloaded from https://academic.oup.com/gji/article-abstract/216/2/1441/5195529 by University of California, Los Angeles user on 06 February 2019

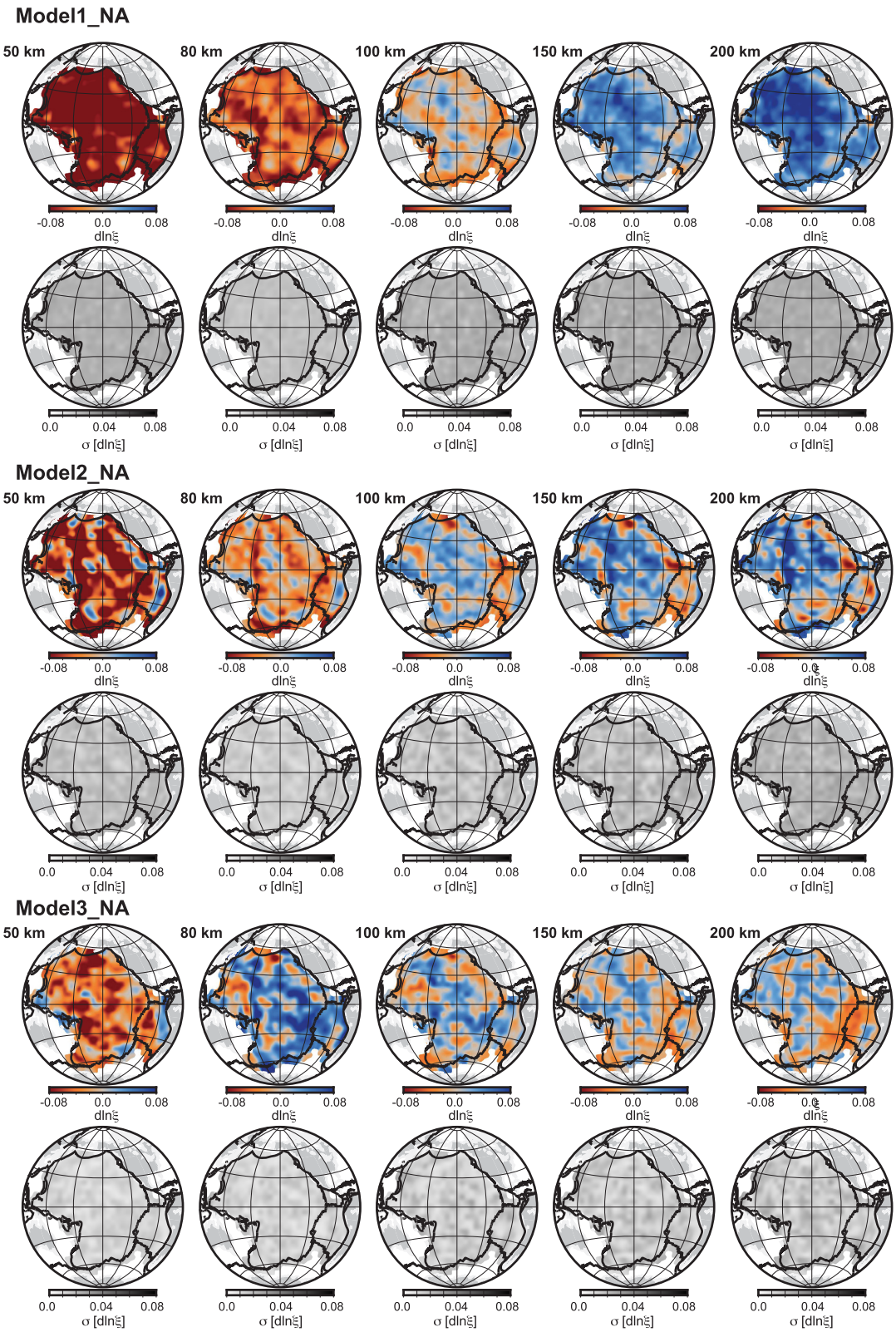

Figure 9. Mean radial anisotropy models and standard deviation obtained by applying the NA to data set 1 (top) and data set 2 (middle) and data set 3 (bottom).

Downloaded from https://academic.oup.com/gji/article-abstract/216/2/1441/5195529 by University of California, Los Angeles user on 06 February 2019

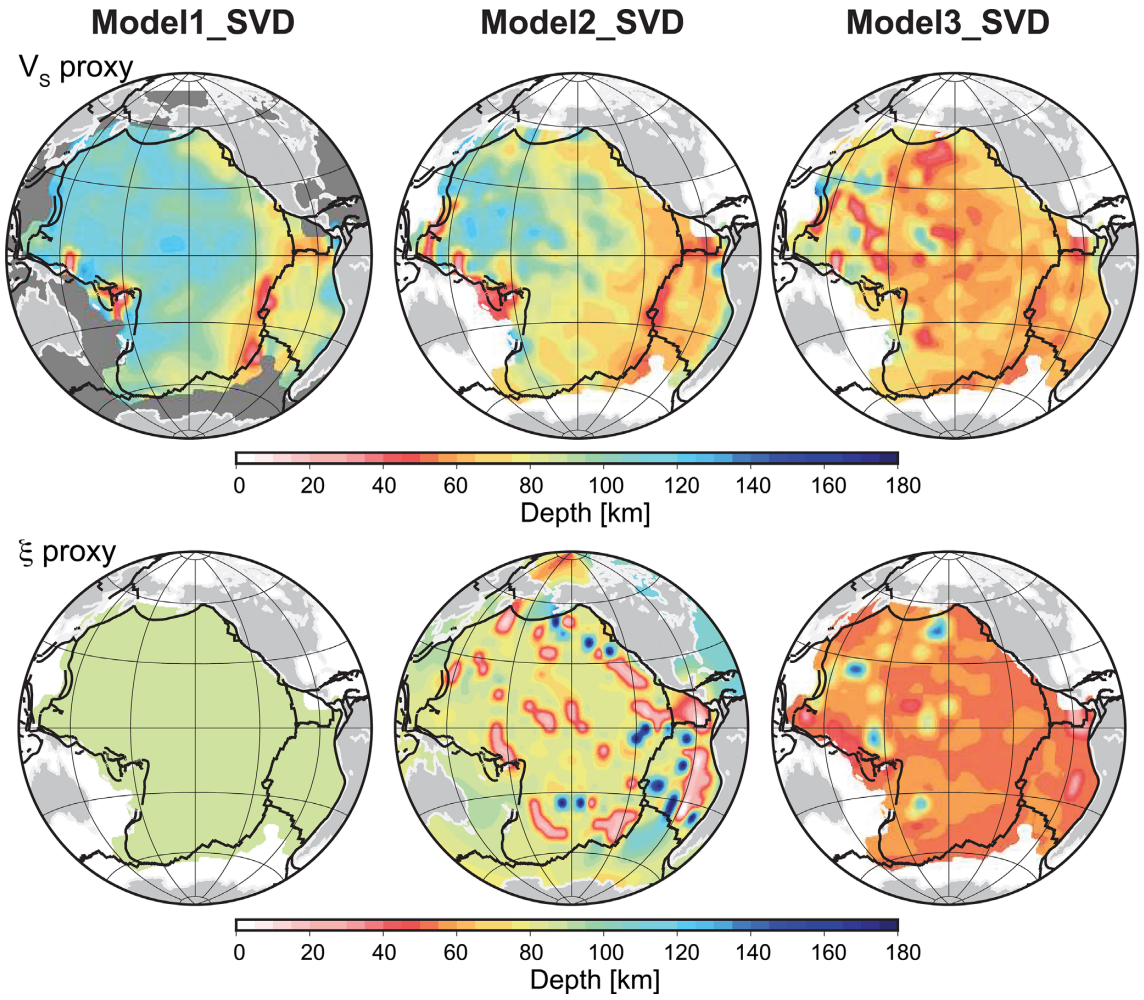

Figure 10. Maps of LAB depth calculated using the depth of the middle of the LVZ (top) and the depth of the largest positive radial anisotropy gradient (bottom) and the models obtained by regularized inversions of data set 1 (left-hand side), data set 2 (middle) and data set 3 (right-hand side).

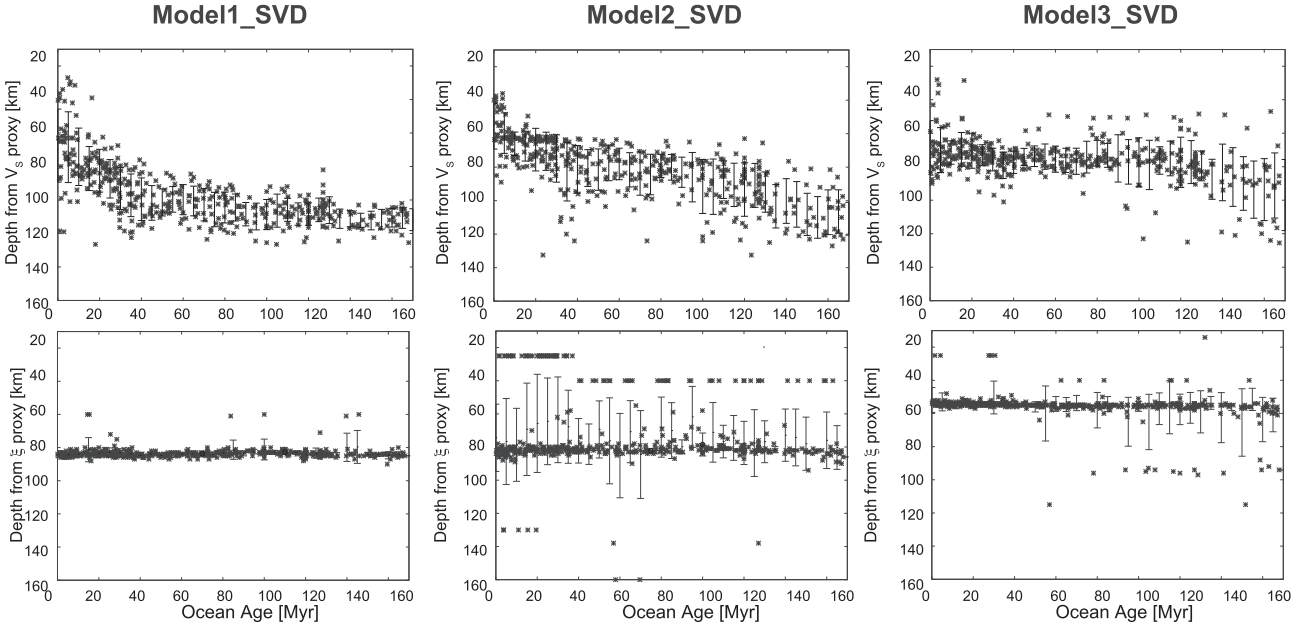

Figure 11. Age dependence of the LAB depth calculated using the depth of the middle of the LVZ (top) and the depth of the largest positive radial anisotropy gradient (bottom) from the models obtained by regularized inversions of data set 1 (left-hand side), data set 2 (middle), and data set 3 (right-hand side). The vertical error bars show one standard deviation representing variations within the model binned every 5 Myr.

Downloaded from https://academic.oup.com/gji/article-abstract/216/2/1441/5195529 by University of California, Los Angeles user on 06 February 2019

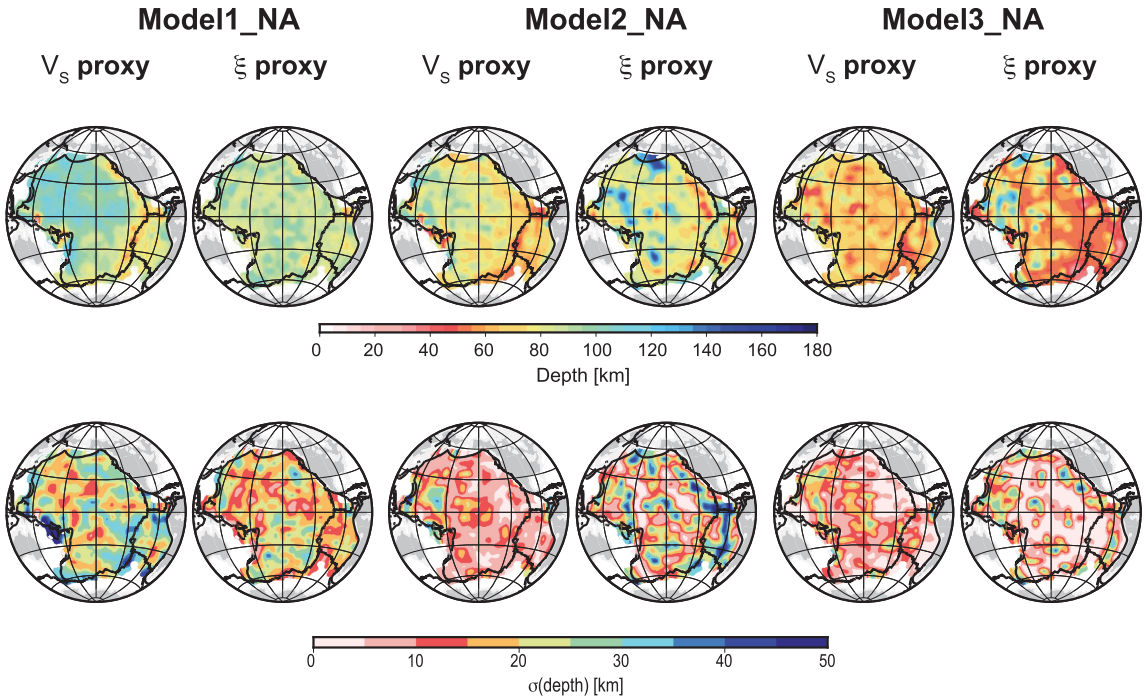

Figure 12. Mean LAB depth (top) and standard deviation (bottom) calculated using the depth of the middle of the LVZ and the depth of the largest positive radial anisotropy gradient and the models obtained by applying NA to data set 1 (left-hand side), data set 2 (middle) and data set 3 (right-hand side).

spreading centres and reaching ∼120 km below the oldest part of the plate. Model3_SVD yields a more uniform LAB depth of around 70 km across most of the study region only deepening to ∼120 km under the oldest part of the Pacific.

Interestingly, for data sets 1 and 2, while the shallowest depths for the V_S-defined LAB proxy are located near the youngest parts of the ocean, these depths are greater than those found in previous work (Burgos *et al.* 2014) and with a strong scatter for similar ages across the study area. This is also the case for older crustal ages, for which our results give generally deeper LAB depths than found by Burgos *et al.* (2014). We note that Burgos *et al.* (2014) employed a different V_S-defined LAB proxy than ours – they used the depth of the maximum negative $\partial V_S/\partial z$ – but we verified that using the same definition with our models does not affect our LAB depth estimates. While our larger LAB depth estimates could be the result of artefacts introduced by the various authors during the construction of their phase velocity maps, the fact that this is occurring with two data sets obtained with different measurement and inversion techniques suggests this signal is robust.

Both Figs 10 and 11 demonstrate that the depth of largest positive $\partial\xi/\partial z$ is generally uniform across the Pacific with little-to-no age variation for all data sets employed, but the depth at which the maximum occurs does depend on the data set. For Model1_SVD, this depth is around 80–90 km, in agreement with results by Burgos *et al.* (2014). A similar depth is found for Model2_SVD, but this model also includes several locations with depths of about 20, 40 and >120km scattered across the Pacific, with no clear age dependence. With group velocities (Model3_SVD), the depth proxy is shallower, around 55 km, as already suggested by Fig. 9.

Fig. 11 clearly shows that there is a very little scatter in the depth of the maximum $\partial\xi/\partial z$, regardless of the data set. This could be interpreted as evidence for an age-independent ξ-based proxy even if the depth of the LAB proxy itself depends on the data set. Before drawing conclusions, it is however essential to look at the statistical distributions of all possible ξ models to determine the robustness of these results. We were able to take advantage of the model space search approach employed to determine quantitative uncertainties on the depth of the two LAB depth proxies examined in this paper. For each grid cell, we drew random model spline coefficients $\mathrm{dln}V_S^i$ and $\mathrm{dln}\,\xi^i$ from their PDDFs to reconstruct a suite of $V_S(r)$ and $\xi(r)$ models, and for each of these models we calculated the depth of the LAB using our two proxies. This yielded distributions of LAB depths at each grid cell, from which a mean depth and standard deviation could be calculated. These are represented in Fig. 12.

As in the SVD inversions, the mean LAB depth resulting from the application of the NA to data set 1 and using the velocity proxy is relatively shallow at ridges and increases towards the older ocean, and the values obtained in the youngest parts of the Pacific are deeper (around 60 km) than usually expected from thermal cooling models. The uncertainty map reveals significant uncertainties with a standard deviation of around 10–15 km in the younger part of the Pacific and 15–20 km elsewhere. The mean depth resulting from $\partial\xi/\partial z$ and data set 1 is relatively uniform with values of 70–90 km and uncertainties of 5–25 km.

With data set 2, the middle of the velocity decrease interval yields a relatively deep LAB of about 50 km at the EPR and error bars of about 5 km. The standard deviation increases to about 20 km towards the older plate. The mean value obtained from $\partial\xi/\partial z$ is around 80 km with an average error of 5–15 km, similar to the results obtained from data set 1. Some lateral variations were also found, but they do not appear correlated with crustal age and because they are associated with larger uncertainties, they are likely not significant.

Downloaded from https://academic.oup.com/gji/article-abstract/216/2/1441/5195529 by University of California, Los Angeles user on 06 February 2019

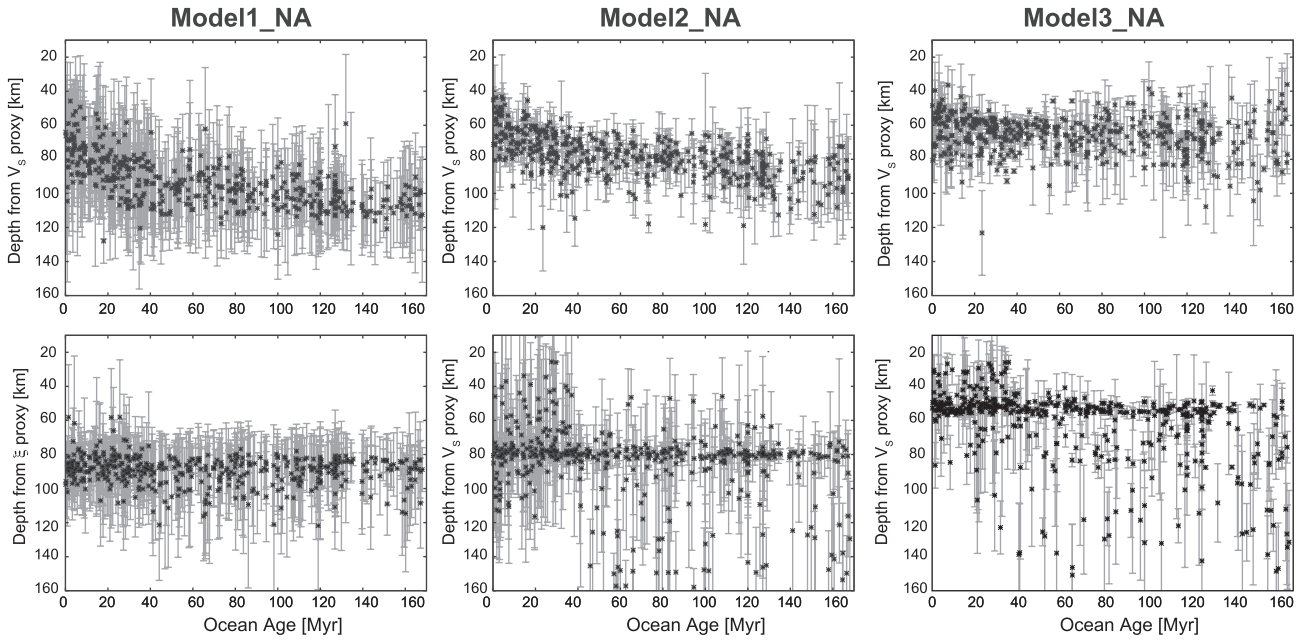

Figure 13. Age dependence of the LAB depth calculated using the depth of the middle of the LVZ (top) and the depth of the largest positive radial anisotropy gradient (bottom) from the models obtained by applying the NA to the three data sets. The mean of the LAB depth distribution calculated at every grid cell is shown with one standard deviation.

With data set 3, the mean LAB depth based on the V_S proxy displays larger values in the western Pacific than near ridges, and values close to 65 km over a large part of the Pacific. Uncertainties in this case are small (<5km) over the northeastern Pacific, rising to 15–20 km in the northwestern part of the study region. The ξ proxy is shallow over a broad section of the Pacific, similar to the SVD results, with values near 50 km, and displays a few locations around 100–120 km in the oldest Pacific. Uncertainties on the ξ proxy are under 5 km over much of the region, though several isolated locations have much larger error bars of 30–40 km.

The mean and standard deviation of these proxies are also represented as a function of crustal age in Fig. 13. Similar to Fig. 11, we plotted the mean and standard deviation for each proxy at every grid cell sorted by increasing seafloor age. Overall, the LAB depths obtained have uncertainties so large that the results from the three data sets are more compatible than it first appears by looking at the SVD results only. We also note that the LAB depths inferred from radial anisotropy have uncertainties of the order of 80–100km, which is probably reflecting the limited depth resolution. In addition, the uncertainties on the radial anisotropy models are sufficiently large that we cannot rule out the existence of a model that would yield an age-dependent $\partial\xi/\partial z$ compatible with the V_S-based proxy. We thus cannot readily conclude that the anisotropy and the velocity model proxies yield different LAB depths or are seeing different properties of the mantle as proposed by previous authors (Hier-Majumder & Drombosky 2015; Hansen *et al.* 2016; Hedjazian *et al.* 2017). We also conclude that radial anisotropy is likely not a good proxy for the LAB because of resolution issues.

4.4 Discussion

Our inversions confirm that oceanic lithosphere–asthenosphere shear wave speed structure and proxies of the LAB vary systematically with crustal age. As discussed in the introduction, there are a number of outstanding questions about the variation in LAB depth with age. By comparing our V_S models against synthetic velocity models, we evaluate the following: (1) Can lithosphere–asthenosphere velocities be explained purely with solid-state thermal effects? (2) Or is an additional signature of either the presence of melt or major-element depletion and dehydration of the mantle due to melting below the ridge required? (3) Can the results be used to discriminate between the end-member models of plate or HSC of oceanic lithosphere with age? (4) Some previous work indicates that the potential temperature below the Pacific may be higher than below other oceans (Goes *et al.* 2013); do the surface wave velocities corroborate this?

We computed synthetic seismic velocities for a set of half-space and plate cooling models (Fig. 14 and Fig. S7, Supporting Information). Thermal parameters were taken from McKenzie *et al.* (2005) (as described in Goes *et al.* 2012), yielding HSC and plate models that reasonably match global bathymetry and flow data as a function of cooling age, for mantle potential temperatures of 1315 °C. We also tested models with a hotter potential temperature of 1415 °C, which provides better fits to Pacific differential *PP-P* and *SS-S* traveltimes (Goes *et al.* 2013).

The temperature structures were converted to seismic velocities using the code PerPleX (Connolly 2005) with the thermodynamic database from Xu *et al.* (2008) to compute elastic parameters and density and with additional correction for anelastic effects as in Goes *et al.* (2012). Two anelasticity models with different temperature- and pressure-dependence were tested: model Q_g, a combined experimental, empirical model similar to those that have been previously used to reconcile V_P, V_S and heatflow observations in a range of tectonic settings (Goes *et al.* 2000; Shapiro & Ritzwoller 2004), and model Q_J, based on experimental parameters from Jackson & Faul (2010). Differences

Downloaded from https://academic.oup.com/gji/article-abstract/216/2/1441/5195529 by University of California, Los Angeles user on 06 February 2019

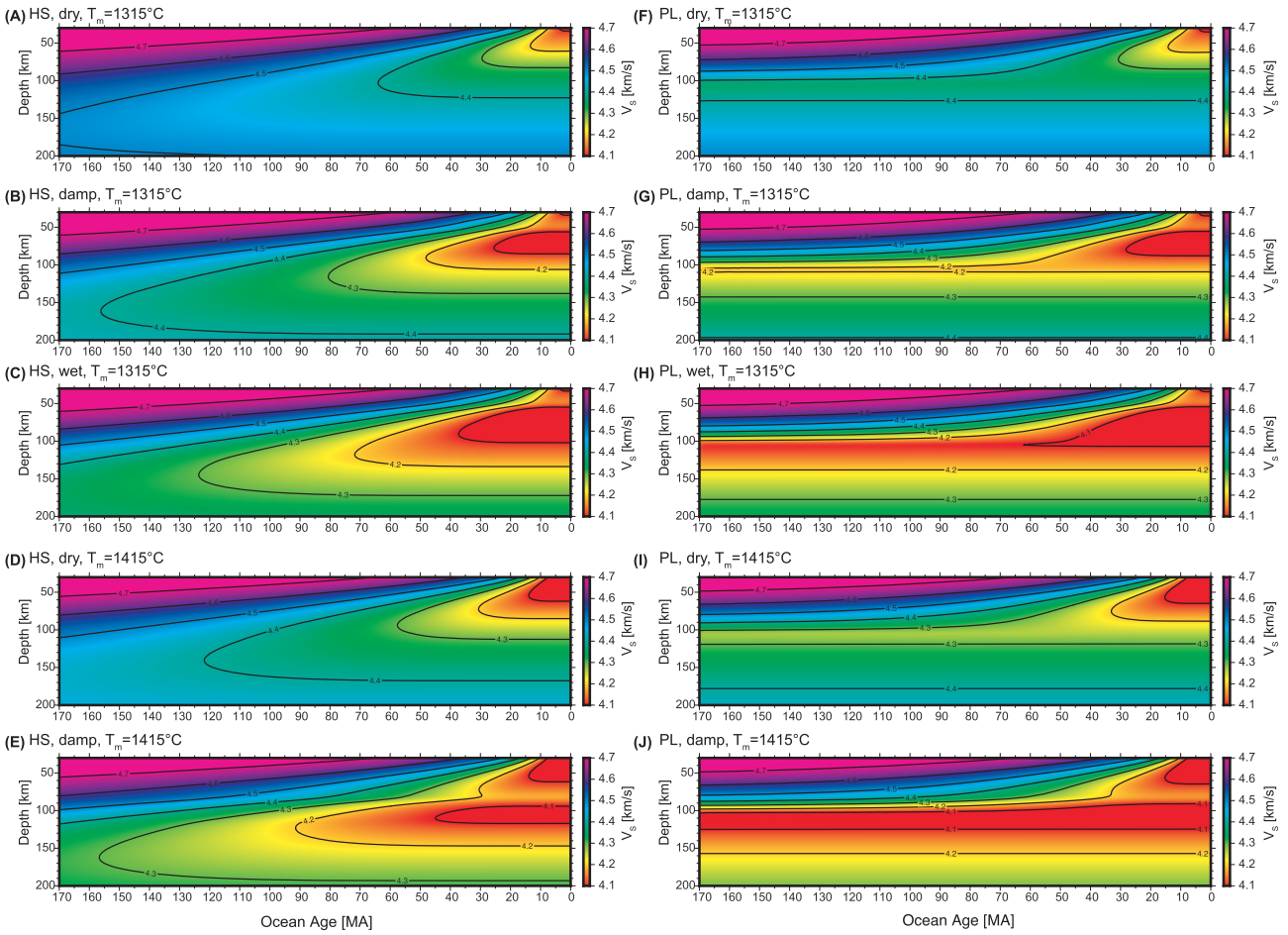

Figure 14. Synthetic velocity models from Goes *et al.* (2012) using empirical attenuation model Q_g. We determined V_S in five cases for each cooling model (HSC on the left and plate model on the right): a dry mantle with potential temperature $T_\mathrm{m} = 1315\,^\circ$C (A and F), a damp mantle with $T_\mathrm{m} = 1315\,^\circ$C (B and G), a wet mantle with $T_\mathrm{m} = 1315\,^\circ$C (C and H), a dry but hotter mantle with $T_\mathrm{m} = 1415\,^\circ$C (D and I) and a damp mantle with $T_\mathrm{m} = 1415\,^\circ$C (E and J). Other thermal parameters were chosen to match those of McKenzie *et al.* (2005).

between the attenuation models are discussed more extensively in Goes *et al.* (2012), but Q_g is semi-empirical and uses homologous temperature (i.e. T/T_melt) in the Arrhenius term to capture temperature and pressure dependence, while Q_J is fully based on experimental measurements of attenuation and uses an Arrhenius term in terms of activation energy and volume, although activation volume cannot be well constrained by the experiments. Q_J is less temperature and pressure dependent, thus predicting a somewhat lower range of velocities as a function of lithospheric age than Q_g. The pressure dependence in Q_J leads to a smaller increase in velocity with depth than in model Q_g. In model Q_g, the minimum attenuation values employed, directly below the ridge, are close to but above 20 for all models we tested. For model Q_J, grainsize is set to a constant 1 cm (see also discussion in Abers *et al.* 2014). Synthetic models are shown for a frequency of 20s (Fig. 14 for Q_g and Fig. S7 of the Supporting Information for Q_J) and comparisons are very similar when we account for the variation of velocity with frequency.

For composition, all models include the effect of major element depletion of the mantle residue due to melting, implemented as a gradient from a peridotitic composition below the depth where (hydrous) melting starts to a fully harzburgitic composition after 20 per cent melt has been extracted. Melting is assumed to occur under the ridge and the dehydrated and melt-depleted material is subsequently advected away from the ridge. Even below the ridge, the depth of dehydration is quite constant, as can be seen in the 2-D models in Goes *et al.* (2012). Because the surface waves used in this paper do not have the resolution to resolve detailed structure below the ridge, we impose the dehydration depths that we obtained from the 2-D models of Goes *et al.* (2012) on the simple ocean cooling models applied here.

The melting conditions depend on potential temperature and whether models are assumed to be dry, damp (1000 H/10^{6}Si) or wet (3000 H/10^{6}Si) and are taken from the dynamic spreading models computed in Goes *et al.* (2012). The presence of water is assumed to affect attenuation (see Goes *et al.* 2012), although the presence of water itself may not actually lower attenuation, but rather redox conditions could be responsible (Cline *et al.* 2018), which, at least in subduction settings, may correlate with water content (Kelley & Cottrell 2009). Oceanic mantle is on average likely somewhat damp (Hirth & Kohlstedt 1996). We also consider dry models, because of the above arguments about sensitivity of Q to water (Cline *et al.* 2018) and, in addition, Abers *et al.* (2014) argue that hydrous weakening effects on attenuation are offset by enhanced grain growth. For the models that assume water is present, dehydration occurs between the depths where the hydrous solidus

Downloaded from https://academic.oup.com/gji/article-abstract/216/2/1441/5195529 by University of California, Los Angeles user on 06 February 2019

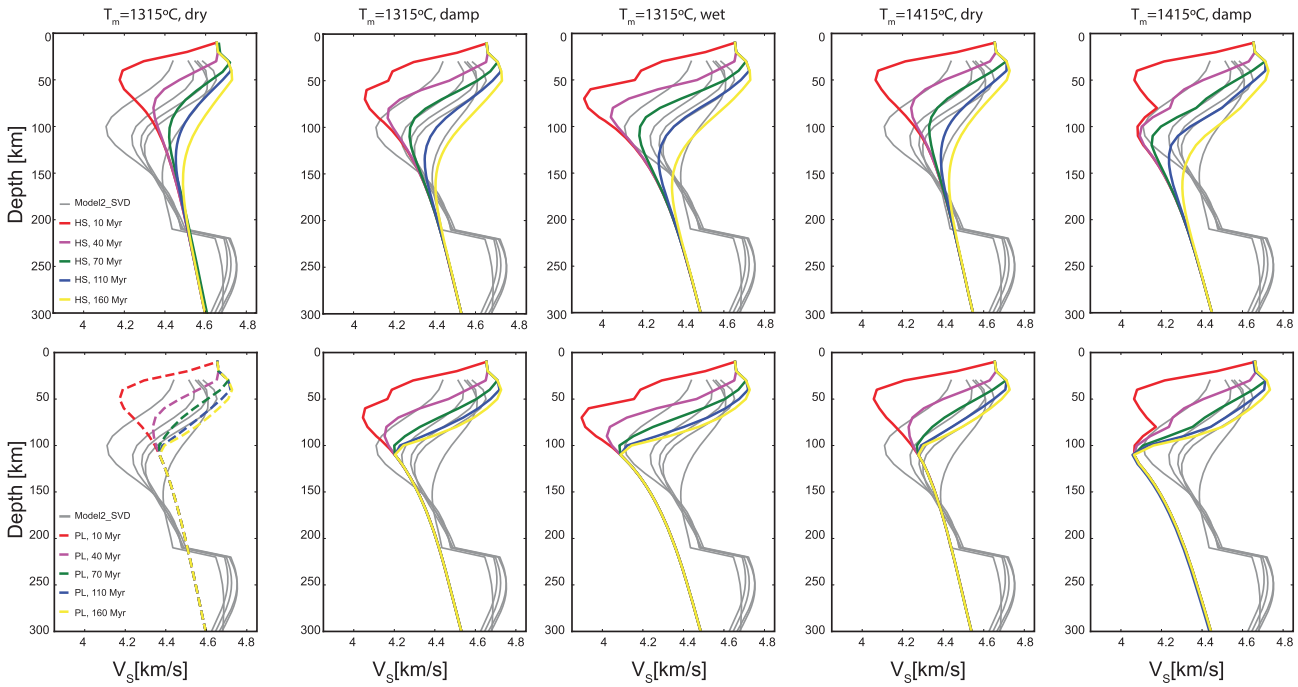

Figure 15. Comparison between velocity depth profiles obtained from the synthetic V_S models described in Fig. 14 for different ocean floor ages (the coloured curves) and Q_g and obtained from the V_S model obtained by regularized inversion of data set 2 (the grey curves) plotted for the same age bins as the synthetic models. Synthetic models for half-space cooling models are shown in the top panels and those for plate models are displayed in the bottom panels.

and dry solidus are crossed (85 and 52 km, respectively, for a damp 1315 °C mantle). Fig. S8 of the Supporting Information depicts the depth intervals in which dehydration occurs in the plate and HSC models with mantle potential temperatures of 1315 and 1415 °C. None of the synthetic models incorporate any effects of the presence of melt, which would lower velocities, at least directly below the ridge, and likely enhance attenuation (Eilon & Abers 2017). Note that enhanced attenuation due to hydration plus decreased attenuation upon dehydration during melting might explain the double low-velocity zone observed in regional surface wave tomography below the East Pacific Rise (Dunn & Forsyth 2003), in which case the lower zone occurs in hydrated, solid-state asthenosphere and the upper zone is due to the presence of melt in a largely dehydrated mantle (Goes *et al.* 2012). As we will show below, a process that lowers attenuation (increases Q) during melting would also help explain the Pacific-wide shear wave velocities with age.

We performed resolution tests using these synthetic V_S models as input with data set 2, and determined that our regularized inversion scheme was able to recover the input models relatively well, though a slight deepening of the low-velocity zone is visible in some of the output models and the inversion scheme tends to overestimate V_S at lithospheric depths around 10–20 Myr old (Figs S9–S12, Supporting Information). In Fig. 15, we compare synthetic V_S depth profiles for model Q_g for different crustal ages with the velocity profiles resulting from regularized inversion of data set 2 for the same ages. Equivalent figures for model Q_g with data sets 1 and 3 and for model Q_J with data set 2 can be found in the Supporting Information Figs S13–S15. Tomographic imaging and uncertainties in the tomographic solutions are expected to cause differences between thermal and tomographic profiles even if structures would be identical, as shown in Figs S9–S12 and Fig. S16 (Supporting Information). However, bearing in mind these uncertainties, several differences between the synthetic and tomographic profiles are noteworthy:

(1) The models without any melt but with hydration effects on Q predict an asthenosphere that is easily slow enough to match the tomographic results. Dry models are too fast and predict velocity minima that are significantly too shallow below younger lithosphere. Lower asthenospheric velocities could, of course, also be obtained in a dry asthenosphere by adding an effect of melt below lithosphere of at least all ages $\leq$70 Myr. However, melt would not help with the next point.

(2) The effects on attenuation of dehydration by melting deepen the velocity minimum below young lithosphere and improve the fit of velocity-age trends. An additional velocity-lowering effect of the presence of melt is expected locally below the ridge, but would not be observable with the type of data used here (Goes *et al.* 2012). If the asthenospheric velocity minimum was the result of the presence of melt instead of being associated with hydration, it is not clear why attenuation would be reduced and velocities increased above depths where significant melting starts below the ridge.

(3) The profiles in Fig. 15 clearly show that the differences in velocity for different ages in our tomographic model persist to greater depths than the plate thickness in the plate-cooling models. HSC models predict differences in V_S down to depths of ~175 km, which matches our tomographic results better. From this we conclude that our velocity models are best represented by half-space type cooling.

Downloaded from https://academic.oup.com/gji/article-abstract/216/2/1441/5195529 by University of California, Los Angeles user on 06 February 2019

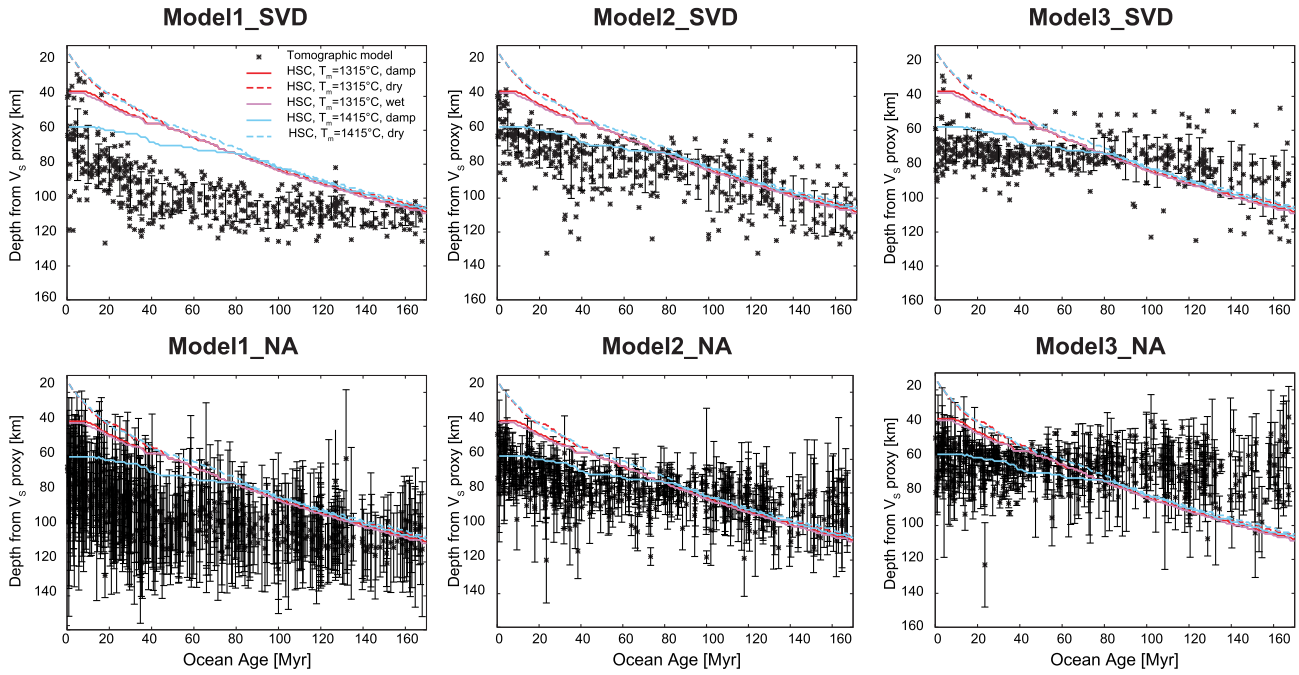

Figure 16. Comparison between LAB depth estimates from our V_S tomographic models and from synthetic velocity models calculated as following Goes *et al.* (2012). The LAB depth proxy is calculated using the depth of the middle of the low-velocity zone. The tomographic models used were obtained from data set 1 (left-hand side), data set 2 (middle) and data set 3 (right-hand side). Models obtained by regularized inversion are displayed on top and models obtained using the NA are shown at the bottom. The vertical error bars are the same as in Figs 11 and 13. The coloured curves represent the LAB depth proxy calculated from the synthetic velocities shown in Fig. 14 and determined for half-space cooling models and Q_g.

(4) Wetter and/or hotter models move the velocity minima to larger depths, yielding the best agreement with the depths from the tomographic models. The hot and wet models also predict lower velocities below the asthenosphere than found in the tomographic inversion, although these differences may at least, in part, be affected by uncertainties in the depth-dependence of attenuation and by limited resolutions of the data at depths exceeding 200 km.

In Fig. 16 we compare our V_S-defined LAB depth proxy determined from our tomographic models and from the synthetic velocity models of Goes *et al.* (2012) calculated for HSC and attenuation model Q_g. We focus on HSC models from here on since they explain our V_S models better than plate models, as discussed above. We see that, for all three data sets and the regularized inversions, the LAB depth for the youngest oceans is best explained by a damp and hot ($T_\mathrm{m} = 1415\,^\circ$C) mantle. The main reason for this preference is that the higher degree of melting predicted by this model leads to a thicker dehydrated layer, thus depressing the asthenospheric velocity minimum. All tomographic models, including those within the error bars obtained with the NA, prefer structures with velocity minima on the deeper end of those our forward thermal models predict. For attenuation model Q_J (Fig. S17, Supporting Information), both a hot ($T_\mathrm{m} = 1415\,^\circ$C) and a $T_\mathrm{m} = 1315\,^\circ$C wet model predict deep enough velocity minima. However, the increase of velocity with depth below 200 km is better matched by the pressure dependence in model Q_g than model Q_J, and this pressure dependence largely offsets the deepening of the velocity minimum for the 1315 °C wet model. Absolute velocities are too uncertain to discriminate between mantle temperatures. However, the comparisons indicate a strong preference for structures in which dehydration leads to a less attenuating layer down to about 80 km depth overlying a more attenuating asthenosphere, as predicted by the hotter mantle models.

Although the tomographic models resulting from data sets 1 and 3 are not matched as well as by the synthetic model trends as the models obtained from data set 2 (Fig. 16), all data sets are consistent with a continued trend of lithospheric cooling until old ages, and all three data sets indicate LAB-age gradients that are more compatible with those from the models where depletion by melting leads to decreased attenuation. Our results therefore suggest no significant fractions of melt are needed to explain the shear wave velocities (although uncertainties are large enough that some amount of melt could be present). This is consistent, as pointed out by Goes *et al.* (2012), with petrological constraints predicting that melt is efficiently removed at asthenospheric depths (Asimow *et al.* 2004). This would indicate that other mechanisms than melt may be necessary to explain or at least contribute to the existence of the Gutenberg discontinuity, for example, associated with fabrics that form due to the melting that occurs below the ridge (Hansen *et al.* 2016; Hedjazian *et al.* 2017), which is also supported by the azimuthal anisotropy results of Beghein *et al.* (2014). Finally, we note that even though our modelling does not require melt, we cannot preclude its presence given the large uncertainties we obtained and accounting for the fact that not all seismological observations can be explained without melt (Schmerr 2012; Cobden *et al.* 2018).

Downloaded from https://academic.oup.com/gji/article-abstract/216/2/1441/5195529 by University of California, Los Angeles user on 06 February 2019

5 CONCLUSIONS

We applied a Bayesian approach to various surface wave data sets to constrain radial anisotropy and shear wave velocities under the Pacific plate and determine the depth of the LAB using various proxies calculated from our tomographic models. Our results show that, while regularized inversion results can yield different LAB depth depending on the data set employed, the uncertainties on the models are large and the resulting LAB depth proxies are, in fact, compatible with one another. Radial anisotropy models are poorly constrained and we cannot conclude that they require different LAB depth estimates than isotropic velocity models. In addition, testing our velocity models against the synthetic models of Goes *et al.* (2012) for half-space and plate models showed that our results are best explained by HSC models that include a decrease in attenuation due to dehydration by melting at the ridge than by dry models or plate models. The imaged depths of the asthenospheric velocity minimum are deeper than predicted for a dry mantle and most consistent with the depths predicted for a damp, 1415 °C mantle where higher degrees of melting lead to a thicker dehydrated layer than in a 1315 °C mantle. The asthenospheric low velocities could also be explained with the presence of melt, but the observed velocity-age trends are not easily explained by melt effects. In addition, given the large uncertainties in the velocity- and anisotropy-based proxies for all data sets, we cannot reject the hypothesis that the different proxies are all compatible with a thermally controlled, that is, age-dependent LAB.

ACKNOWLEDGEMENTS

We wish to thank Göran Ekström, Karin Visser and Jeannot Trampert for making the surface wave velocity maps freely available online at http://www.geo.uu.nl/~jeannot/My_web_pages/Downloads.html and http://www.ldeo.columbia.edu/~ekstrom/, and Malcom Sambridge for sharing his Neighbourhood Algorithm. We also thank Laura Cobden and an anonymous reviewer for their helpful suggestions. Partial derivatives were calculated using program MINEOS (available on the CIG website at http://www.geodynamics.org/), and figures were made using the Generic Mapping Tool. Calculations were made on CB's computer cluster, which was funded by NSF grant #0949255. This is the Lunar and Planetary Institute Contribution Number LPI-002145.

REFERENCES

Abers, G.A., Fischer, K.M., Hirth, G., Wiens, D.A., Plank, T., Holtzman, B.K., McCarthy, C. & Gazel, E., 2014. Reconciling mantle attenuation-temperature relationships from seismology, petrology, and laboratory measurements, *Geochem. Geophys. Geosys,* **15**.

Amante, C. & Eakins, B., 2009. Etopo1 1 arc-minute global relief model: procedures, data sources and analysis, in *NOAA Technical Memorandum NESDIS NGDC-24,* National Geophysical Data Center, NOAA.

Anderson, D.L. & Sammis, C., 1970. Partial melting in the upper mantle, *Phys. Earth planet. Inter.,* **3,** 41–50.

Asimow, P.D., Dixon, J.E. & Langmuir, C.H., 2004. A hydrous melting and fractionation model for mid-ocean ridge basalts: Application to the Mid-Atlantic Ridge near the Azores, *Geochem., Geophys., Geosyst.,* **5**.

Babuška, V. & Cara, M., 1991. *Seismic Anisotropy in the Earth, Modern Approaches in Geophysics, vol. 10,* Springer.

Bagley, B. & Revenaugh, J., 2008. Upper mantle seismic shear discontinuities of the Pacific, *J. geophys. Res.,* **113**(B12), 301.

Bartzsch, S., Lebedev, S. & Meier, T., 2011. Resolving the lithosphere–asthenosphere boundary with seismic Rayleigh waves, *Geophys. J. Int.,* **186**(3), 1152–1164.

Bassin, C., Laske, G. & Masters, G., 2000. The current limits of resolution for surface wave tomography in North America, *EOS Trans., Am. geophys. Un.,* **81,** F897.

Bayes, M. & Price, M., 1763. An essay towards solving a problem in the doctrine of chances. By the late rev. Mr. Bayes, FRS communicated by Mr. Price, in a letter to John Canton, AMFRS, in *Phil. Trans. R. Soc. Lond.,* **53,** 370–418.

Becker, T.W., Conrad, C.P., Schaeffer, A.J. & Lebedev, S., 2014. Origin of azimuthal seismic anisotropy in oceanic plates and mantle, *Earth planet. Sci. Lett.,* **401,** 236–250.

Beghein, C., 2010. Radial anisotropy and prior petrological constraints: a comparative study, *J. geophys. Res.,* **115**(B3).

Beghein, C., Resovsky, J. & Van der Hilst, R.D., 2008. The signal of mantle anisotropy in the coupling of normal modes, *Geophys. J. Int.,* **175**(3), 1209–1234.

Beghein, C. & Trampert, J., 2003. Robust normal mode constraints on inner-core anisotropy from model space search, *Science,* **299**(5606), 552–555.

Beghein, C., Yuan, K., Schmerr, N. & Xing, Z., 2014. Changes in seismic anisotropy shed light on the nature of the Gutenberg discontinuity, *Science,* **343**(6176), 1237–1240.

Boschi, L. & Ekström, G., 2002. New images of the Earth's upper mantle from measurements of surface wave phase velocity anomalies, *J. geophys. Res.,* **107**(B4).

Bozdag, E. & Trampert, J., 2008. On crustal corrections in surface wave tomography, *Geophys. J. Int.,* **172,** 1066–1082.

Burgos, G., Montagner, J.-P., Beucler, E., Capdeville, Y., Mocquet, A. & Drilleau, M., 2014. Oceanic lithosphere–asthenosphere boundary from surface wave dispersion data, *J. geophys. Res.,* **119**(2), 1079–1093.

Chang, S.-J., Ferreira, A.M., Ritsema, J., van Heijst, H.J. & Woodhouse, J.H., 2014. Global radially anisotropic mantle structure from multiple datasets: a review, current challenges, and outlook, *Tectonophysics,* **617,** 1–19.

Chang, S.-J., Ferreira, A.M., Ritsema, J., van Heijst, H.J. & Woodhouse, J.H., 2015. Joint inversion for global isotropic and radially anisotropic mantle structure including crustal thickness perturbations, *J. geophys. Res.,* **120**(6), 4278–4300.

Chave, A.D., Von Herzen, R.P., Poehls, K.A. & Cox, C.S., 1981. Electromagnetic induction fields in the deep ocean north-east of Hawaii: implications for mantle conductivity and source fields, *Geophys. J. Int.,* **66**(2), 379–406.

Cline, C.J., II, Faul, U.H., David, E.C., Berry, A.J. & Jackson, I., 2018. Redox-influenced seismic properties of upper-mantle olivine, *Nature,* **555,** 355–358.

Cobden, L., Trampert, J. & Fichtner, A., 2018. Insights on upper mantle melting, rheology and anelastic behaviour from seismic shear-wave tomography, *Geochem. Geophys. Geosyst.,* **19,** 3892–3916.

Connolly, J.A.D., 2005. Computation of phase equilibria by linear programming: a tool for geodynamic modeling and its application to subduction zone decarbonation, *Earth planet. Sci. Lett.,* **236,** 524–541.

Courtier, A. & Leahy, G., 2011. Joint receiver function/SCS reverberation analysis for examining discontinuity structure beneath ocean islands, *Bull. seism. Soc. Am.,* **101**(2), 908–914.

Debayle, E. & Ricard, Y., 2013. Seismic observations of large-scale deformation at the bottom of fast-moving plates, *Earth planet. Sci. Lett.,* **376,** 165–177.

Downloaded from https://academic.oup.com/gji/article-abstract/216/2/1441/5195529 by University of California, Los Angeles user on 06 February 2019

Dunn, R.A. & Forsyth, D.W., 2003. Imaging the transition between the region of mantle melt generation and the crustal magma chamber beneath the southern East Pacific Rise with short-period Love waves, *J. geophys. Res.,* **108**(B7), 2352.

Dziewonski, A.M. & Anderson, D.L., 1981. Preliminary reference Earth model, *Phys. Earth planet. Inter.,* **25**(4), 297–356.

Eaton, D.W., Darbyshire, F., Evans, R.L., Grütter, H., Jones, A.G. & Yuan, X., 2009. The elusive lithosphere–asthenosphere boundary (LAB) beneath cratons, *Lithos,* **109**(1), 1–22.

Eilon, Z.C. & Abers, G.A., 2017. High seismic attenuation at a mid-ocean ridge reveals the distribution of deep melt, *Sci. Adv.,* **3**(5).

Ekström, G., 2011. A global model of Love & Rayleigh surface wave dispersion and anisotropy, 25–250 s, *Geophys. J. Int.,* **187,** 1668–1686.

Faul, U.H. & Jackson, I., 2005. The seismological signature of temperature and grain size variations in the upper mantle, *Earth planet. Sci. Lett.,* **234**(1–2), 119–134.

Ferreira, A.M.G., Woodhouse, J.H., Visser, K. & Trampert, J., 2010. On the robustness of global radially anisotropic surface wave tomography, *J. geophys. Res.,* **115**(B4), 1–16.

Fichtner, A., Trampert, J., Cupillard, P., Saygin, E., Taymaz, T., Capdeville, Y. & Villaseñor, A., 2013. Multiscale full waveform inversion, *Geophys. J. Int.,* **194**(1), 534–556.

Filloux, J.H., 1980. Magnetotelluric soundings over the northeast pacific may reveal spatial dependence of depth and conductance of the asthenosphere, *Earth planet. Sci. Lett.,* **46**(2), 244–252.

Fischer, K.M., Ford, H.A., Abt, D.L. & Rychert, K., 2010. The lithosphere–asthenosphere boundary, *Annu. Rev. Earth Planet. Sci.,* **38**(1), 551–575.

Forsyth, D.W. *et al.*, 1998. Imaging the deep seismic structure beneath a mid-ocean ridge: the MELT experiment, *Science,* **280,** 1215–1218.

Gaherty, J.B., Jordan, T.H. & Gee, L.S., 1996. Seismic structure of the upper mantle in a central pacific corridor, *J. geophys. Res.,* **101,** 22 291–22 309.

Goes, S., Armitage, J., Harmon, N., Smith, A. & Huismans, R., 2012. Low seismic velocities below mid-ocean ridges: attenuation versus melt retention, *J. geophys. Res.,* **117**(B12).

Goes, S., Eakin, C.M. & Ritsema, J., 2013. Lithospheric cooling trends and deviations in oceanic PP-P and SS-S differential traveltimes, *J. geophys. Res.,* **118**.

Goes, S., Govers, R. & Vacher, P., 2000. Shallow upper mantle temperatures under Europe from *P* and *S* wave tomography, *J. geophys. Res.,* **105**(B5), 11 153–11 169.

Gripp, A.E. & Gordon, R.G., 1990. Current plate velocities relative to the hotspots incorporating the NUVEL-1 global plate motion mode, *Geophys. Res. Lett.,* **17**(8), 1109–1112.

Gripp, A.E. & Gordon, R.G., 1992. Young tracks of hotspots and current plate velocities, *Geophys. J. Int.,* **150**(2), 321–361.

Hansen, L.N., Qi, C. & Warren, J.M., 2016. Olivine anisotropy suggests Gutenberg discontinuity is not the base of the lithosphere, *Proc. Natl. Acad. Sci. USA,* **113,** 10 503–10 506.

Harmon, N., Forsyth, D.W. & Weeraratne, D.S., 2009. Thickening of young Pacific lithosphere from high-resolution Rayleigh wave tomography: a test of the conductive cooling mode, *Earth planet. Sci. Lett.,* **278,** 96–106.

Hedjazian, N., Garel, F., Davies, D.R. & Kaminski, E., 2017. Age-independent seismic anisotropy under oceanic plates explained by strain history in the asthenosphere, *Earth planet. Sci. Lett.,* **460,** 135–142.

Hier-Majumder, S. & Drombosky, T., 2015. Development of anisotropic contiguity in deforming partially molten aggregates: 2. Implications for the lithosphere–asthenosphere boundary, *J. geophys. Res.,* **120,** 764–777.

Hirschmann, M.M., 2010. Partial melt in the oceanic low velocity zone, *Phys. Earth planet. Inter.,* **179,** 60–71.

Hirth, G. & Kohlstedt, D.L., 1996. Water in the oceanic upper mantle: implications for rheology, melt extraction and the evolution of the lithosphere, *Earth planet. Sci. Lett.,* **144**(1), 93–108.

Jackson, I. & Faul, U.H., 2010. Grainsize-sensitive viscoelastic relaxation in olivine: towards a robust laboratory-based model for seismological application, *Phys. Earth planet. Inter.,* **183**(1–2), 151–163.

Karato, S.-I., 2012. On the origin of the asthenosphere, *Earth planet. Sci. Lett.,* **321,** 95–103.

Karato, S.-I. & Jung, H., 1998. Water, partial melting and the origin of seismic low velocity and high attenuation zone in the upper mantle, *Earth planet. Sci. Lett.,* **157,** 193–207.

Karato, S.-I., Jung, H., Katayama, I. & Skemer, P., 2008. Geodynamic significance of seismic anisotropy of the upper mantle: new insights from laboratory studies, *Annu. Rev. Earth Planet. Sci.,* **36,** 59–95.

Kawakatsu, H., Kumar, P., Takei, Y. & Shinohara, M., 2009. Seismic evidence for sharp lithosphere–asthenosphere boundaries of oceanic plates, *Science,* **324**(5926), 499–502.

Kelley, K.A. & Cottrell, E., 2009. Water and the oxidation state of subduction zone magmas, *Science,* **325,** 605–607.

Kustowski, B., Dziewonski, A.M. & Ekström, G., 2007. Nonlinear crustal corrections for normal-mode seismograms, *Bull. seism. Soc. Am.,* **97**(5), 1756–1762.

Laske, G., Masters, G., Ma, Z. & Pasyanos, M., 2013. Update on CRUST1.0 - A 1-degree Global Model of Earth's Crust, in *EGU General Assembly Conference Abstracts, Vol. 15,* Eur. Geosci. Un., Munich, pp. 2658

Lekić, V. & Romanowicz, B., 2011. Inferring upper-mantle structure by full waveform tomography with the spectral element method, *Geophys. J. Int.,* **185**(2), 799–831.

Lizarralde, D., Chave, A., Hirth, G. & Schultz, A., 1995. Northeastern Pacific mantle conductivity profile from long-period magnetotelluric sounding using Hawaii-to-California submarine cable data, *J. geophys. Res.,* **100**(B9), 17 837–17 854.

Love, A.E.H., 1927. *A Treatise on the Mathematical Theory of Elasticity,* Dover.

Lundstrom, C.C., 2003. Uranium-series disequilibria in mid-ocean ridge basalts: observations and models of basalt genesis, *Rev. Mineral. Geochem.,* **52,** 175–214.

Maggi, A., Debayle, E., Priestley, K. & Barruol, G., 2006. Multimode surface waveform tomography of the Pacific ocean: a closer look at the lithospheric cooling signature, *Geophys. J. Int.,* **166**(3), 1384–1397.

Marone, F. & Romanowicz, B., 2007. Non-linear crustal corrections in high-resolution regional waveform seismic tomography, *Geophys. J. Int.,* **170**(1), 460–467.

Masters, G., Woodhouse, H.J. & Freeman, G., 2011. Mineos v1.0.2 [software], in *Computational Infrastructure for Geodynamics*

Matsu'ura, M. & Hirata, N., 1982. Generalized least-squares solutions to quasi-linear inverse problems with a priori information, *J. Phys. Earth,* **30**(6), 451–468.

Ma, Z. & Dalton, C., 2017. Evolution of the lithosphere in the Indian ocean from combined earthquake and ambient noise tomography, *J. geophys. Res.,* **121,** 1–18.

McKenzie, D., Jackson, J. & Priestley, J., 2005. Thermal structure of oceanic and continental lithosphere, *Earth planet. Sci. Lett.,* **233,** 337–349.

Menke, W., 2012. *Geophysical Data Analysis: Discrete Inverse Theory,* 3rd edn, Elsevier, p. 330.

Montagner, J.-P. & Anderson, D.L., 1989. Petrological constraints on seismic anisotropy, *Phys. Earth planet. Inter.,* **54**(1–2), 82–105.

Montagner, J.-P. & Nataf, H.-C., 1986. A simple method for inverting the azimuthal anisotropy of surface waves, *J. geophys. Res.,* **91**(B1), 511–520.

Naif, S., Key, K., Constable, S. & Evans, R.L., 2013. Melt-rich channel observed at the lithosphere–asthenosphere boundary, *Nature,* **495**(7441), 356–359.

Nettles, M. & Dziewoński, A.M., 2008. Radially anisotropic shear velocity structure of the upper mantle globally and beneath north America, *J. geophys. Res.,* **113**(B2).

Nishimura, C.E. & Forsyth, D.W., 1989. The anisotropic structure of the upper mantle in the Pacific, *Geophys. J.,* **96**(2), 203–229.

Olugboji, T.M., Park, J., Karato, S.-i. & Shinohara, M., 2016. Nature of the seismic lithosphere–asthenosphere boundary within normal oceanic mantle from high-resolution receiver functions, *Geochem. Geophys. Geosyst.,* **17**(4), 1265–1282.

Panning, M. & Romanowicz, B., 2006. A three-dimensional radially anisotropic model of shear velocity in the whole mantle, *Geophys. J. Int.,* **167**(1), 361–379.

Downloaded from https://academic.oup.com/gji/article-abstract/216/2/1441/5195529 by University of California, Los Angeles user on 06 February 2019

Panning, M.P., Lekić, V. & Romanowicz, B.A., 2010. Importance of crustal corrections in the development of a new global model of radial anisotropy, *J. geophys. Res.,* **115**(B12), B12325, doi:10.1029/2010jb007520.
Parisi, L. & Ferreira, A.M., 2016. Empirical assessment of the validity limits of the surface wave full ray theory using realistic 3-D Earth models, *Geophys. J. Int.,* **205**(1), 146–159.
Park, J. & Yu, Y., 1992. Anisotropy and coupled free oscillations - simplified models and surface-wave observations, *Geophys. J. R. astr. Soc.,* **110**(3), 401–420.
Parsons, B. & Sclater, J.G., 1977. An analysis of the variation of ocean floor bathymetry and heat flow with age, *J. geophys. Res.,* **82**(5), 803–827.
Revenaugh, J. & Jordan, T.H., 1991. Mantle layering from ScS reverberations: 3. The upper mantle, *J. geophys. Res.,* **96**(B12), 19 781–19 810.
Ritzwoller, M.H., Shapiro, N.M. & Zhong, S.-J., 2004. Cooling history of the Pacific lithosphere, *Earth planet. Sci. Lett.,* **226**(1), 69–84.
Rodi, W., Glover, P., Li, M. & Alexander, S., 1975. A fast, accurate method for computing group-velocity partial derivatives for Rayleigh & Love modes, *Bull. seism. Soc. Am.,* **65**(5), 1105–1114.
Rubin, K.H., Van der Zander, I., Smith, M.C. & Bergmanis, E.C., 2005. Minimum speed limit for ocean ridge magmatism from ^{210}Pb –^{226}Ra –^{230}Th disequilibria, *Nature,* **437,** 534–538.
Rychert, C. & Shearer, P.M., 2011. Imaging the lithosphere–asthenosphere boundary beneath the Pacific using ss waveform modeling, *J. geophys. Res.,* **116**(B07307).
Röhm, A.H.E., Snieder, R.K., Goes, S. & Trampert, J., 2000. Thermal structure of continental upper mantle inferred from *S* wave velocity and surface heat flow, *Earth planet. Sci. Lett.,* **181,** 395–407.
Sakamaki, T. *et al.*, 2013. Ponded melt at the boundary between the lithosphere and asthenosphere, *Nat. Geosci.,* **6**(12), 1041–1044.
Sambridge, M., 1999a. Geophysical inversion with a neighbourhood algorithm-I. Searching a parameter space, *Geophys. J. Int.,* **138**(2), 479–494.
Sambridge, M., 1999b. Geophysical inversion with a neighbourhood algorithm-II. Appraising the ensemble, *Geophys. J. Int.,* **138**(3), 727–746.
Schaeffer, A. J., Lebedev, S. & Becker, T.W., 2016. Azimuthal seismic anisotropy in the Earth's upper mantle and the thickness of tectonic plates, *Geophys. J. Int.,* **207,** 901–933.
Schmerr, N., 2012. The Gutenberg discontinuity: melt at the lithosphere–asthenosphere boundary, *Science,* **335**(6075), 1480–1483.
Shankland, T.J., O'Connell, J.R. & Waff, H.S., 1981. Geophysical constraints on partial melt in the upper mantle, *J. geophys. Res.,* **19**(3), 394–406.
Shapiro, N.M. & Ritzwoller, M.H., 2004. Thermodynamic constraints on seismic inversions, *Geophys. J. Int.,* **157,** 1175–1188.
Smith, D., Ritzwoller, M.H. & Shapiro, N., 2004. Stratification of anisotropy in the Pacific upper mantle, *J. geophys. Res.,* **109**(B11).
Stein, C.A. & Stein, S., 1992. A model for the global variation in oceanic depth and heat flow with lithospheric age, *Nature,* **359**(6391), 123–129.
Stixrude, L. & Lithgow-Bertelloni, C., 2005. Mineralogy and elasticity of the oceanic upper mantle: Origin of the low-velocity zone, *J. geophys. Res.,* **110**(B03204).
Stracke, A., Bourdon, B. & McKenzie, D., 2006. Melt extraction in the Earth's mantle: Constraints from U-Th-Pa-Ra studies in oceanic basalts, *Earth planet. Sci. Lett.,* **244,** 97–112.
Takeuchi, H. & Saito, M., 1972. Seismic surface waves, in *Methods in Computational Physics, Vol. 11,* p. 217–295, ed. Bolt, B., Academic Press
Tharimena, S., Rychert, C. & Harmon, N., 2017b. A unified continental thickness from seismology and diamonds suggests a melt-defined plate, *Science,* **357**(6351), 580–583.
Tharimena, S., Rychert, C., Harmon, N. & White, P., 2017a. Imaging Pacific lithosphere seismic discontinuities - Insights from SS precursor modeling, *J. geophys. Res.,* **122**.
Trampert, J., 1998. Global seismic tomography: the inverse problem and beyond, *Inverse Probl.,* **14**(3), 371.
Visser, K., Trampert, J. & Kennett, B.L.N., 2008a. Global anisotropic phase velocity maps for higher mode Love and Rayleigh waves, *Geophys. J. Int.,* **172**(3), 1016–1032.
Visser, K., Trampert, J., Lebedev, S. & Kennett, B., 2008b. Probability of radial anisotropy in the deep mantle, *Earth planet. Sci. Lett.,* **270**(3–4), 241–250.
Woodhouse, J.H. & Dahlen, F.A., 1978. The effect of a general aspherical perturbation on the free oscillations of the Earth, *Geophys. J. R. astr. Soc.,* **53**(2), 335–354.
Xing, Z. & Beghein, C., 2015. A Bayesian approach to assess the importance of crustal corrections in global anisotropic surface wave tomography, *Geophys. J. Int.,* **203**(3), 1832–1846.
Xu, W., Lithgow-Bertelloni, C., Stixrude, L. & Ritsema, J., 2008. The effect of bulk composition and temperature on mantle seismic structure, *Earth planet. Sci. Lett.,* **275,** 70–79.
Yuan, K. & Beghein, C., 2014. Three-dimensional variations in Love and Rayleigh wave azimuthal anisotropy for the upper 800 km of the mantle, *J. geophys. Res.,* **119**(4), 3232–3255.
Zhang, S. & Karato, S.-i., 1995. Lattice preferred orientation of olivine aggregates deformed in simple shear, *Nature,* **375,** 774–777.

SUPPORTING INFORMATION

Supplementary data are available at *GJI* online.

Figure S1. Example of model space sampling obtained during the first stage of the NA.
Figure S2. Example of PPDFs obtained after running the first part of the NA using $n_s = n_r = 10$ for 20 000 iterations (results of sampling done in the first part of the NA are shown in Fig. S1). The horizontal axes span the entire prior model distributions. The fact that the PPDFs are narrower than the prior shows that the data contained information about the model parameters.
Figure S3. Synthetic tests using data set 1 (Visser *et al.* 2008) for layer thicknesses of 30 km (A & B), 50 km (C & D), 70 km (E & F) and 10 0 km (G & H).
Figure S4. Synthetic tests using data set 2 (Ekstrom *et al.* 2011) for layer thicknesses of 30 km (A & B), 50 km (C & D), 70 km (E & F) and 100 km (G & H).
Figure S5. Synthetic tests using data set 3 (Ekstrom *et al.* 2011) for layer thicknesses of 30 km (A & B), 50 km (C & D), 70 km (E & F) and 100 km (G & H).
Figure S6. Mean relative velocity (top) and radial anisotropy (bottom) perturbations and standard deviations obtained with data set 1 and NA with a model space search centred around PREM (Dziewonski & Anderson 1981).
Figure S7. Synthetic seismic velocities for a half-space (left-hand side) and a plate cooling (right-hand side) model using attenuation model QJ. A combined experimental and empirical model as described in Goes *et al.* (2012). Thermal parameters were taken from McKenzie *et al.* (2005) for mantle potential temperatures of 1315 °C (A–C) and (F–H) and 1415 °C (D–E) and (I–J). In all cases, velocities were determined for a dry mantle (A, D, F and I) and a damp mantle (1000 H/106Si) (B, G, E and J). We also tested a wetter mantle (3000 H/106Si) for the lower temperature case (C and H).

Downloaded from https://academic.oup.com/gji/article-abstract/216/2/1441/5195529 by University of California, Los Angeles user on 06 February 2019

Figure S8. Thermal structures used to compute the forward seismic velocity structures, for 1315 °C (a,c) and 1415 °C (b,d) mantle potential temperatures. Top row (a,b) shows half-space cooling and bottom row (c,d) plate models. Temperature contours are labelled with temperatures in Kelvin. Major-element composition (for anharmonic velocities) and level of hydration (for attenuation models) are assigned based on the results from the ocean ridge spreading models in Goes *et al.* (2012) which included melting effects. These depths are set below the ridge and preserved upon spreading. White lines indicate the depths where hydrous melting and hence dehydration starts (stippled), where dehydration is assumed complete and dry melting and major element depletion starts (small dashes) and where major element depletion is complete (longer dashes). Between these depths, a linear gradient in hydration and in mixing between peridotite and harzburgite compositions is imposed. Due to the higher temperatures in the 1415 °C models, dehydration and major element depletion start and complete at larger depths than in the 1315 °C models.

Figure S9. Synthetic tests using the synthetic HSC VS models of Fig. 14 as input with data set 2.

Figure S10. Synthetic tests using the synthetic plate VS models of Fig. 14 as input with data set 2.

Figure S11. Synthetic tests using the synthetic HSC VS models of Fig. S7 as input with data set 2.

Figure S12. Synthetic tests using the synthetic plate VS models of Fig. S7 as input with data set 2.

Figure S13. Synthetic VS depth profiles for attenuation model Q_g at different crustal ages and velocity profiles resulting from regularized inversion of data set 1 for the same ages.

Figure S14. Synthetic VS depth profiles for attenuation model Q_g at different crustal ages and velocity profiles resulting from regularized inversion of data set 3 for the same ages.

Figure S15. Synthetic VS depth profiles for attenuation model Q_J at different crustal ages and velocity profiles resulting from regularized inversion of data set 2 for the same ages.

Figure S16. Comparison between the output synthetic VS depth profiles (coloured curves) taken from Fig. S9 for different crustal ages and the velocity profiles (the grey curves) resulting from the regularized inversion of data set 2 for the same ages. The output synthetic VS models were obtained by SVD inversion of the data predicted by the synthetic VS model of Goes *et al.* 2012. also shown in Fig. S9, calculated for HS cooling and attenuation model Q_g.

Figure S17. VS-defined LAB depth proxy determined from our tomographic models and from the synthetic velocity models of Goes *et al.* (2012) calculated for HSC and attenuation model Q_J.

Please note: Oxford University Press is not responsible for the content or functionality of any supporting materials supplied by the authors. Any queries (other than missing material) should be directed to the corresponding author for the paper.

Downloaded from https://academic.oup.com/gji/article-abstract/216/2/1441/5195529 by University of California, Los Angeles user on 06 February 2019